Flexural behaviour of the segmental precast concrete decks post-tensioned by GFRP rods

Shahrad Ebrahimzadeh [a], Allan Manalo [a,*], Omar Alajarmeh [a], Xian Yang [a], Charles Dean Sorbello [b], Senarath Weerakoon [b], Reza Hassanli [c], Brahim Benmokrane [d]

[a] Centre for Future Materials (CFM), School of Civil Engineering and Surveying, University of Southern Queensland, Toowoomba 4350, Australia
[b] Maritime Safety Queensland, Department of Transport and Main Roads, Brisbane, QLD 4000, Australia
[c] UniSA STEM, University of South Australia, Mawson Lakes, SA 5095, Australia
[d] University of Sherbrooke, Department of Civil & Building Engineering, Sherbrooke, Quebec J1K 2R1, Canada

ARTICLE INFO

ABSTRACT

This paper introduces an innovative post-tensioned segmental concrete deck system internally reinforced and tied with GFRP reinforcements for application in pontoon decks and other deck structures in aggressive marine environments. Utilisation of the GFRP reinforcements in floating concrete structures is essential because of their non-corrosive characteristics. Six large-scale segmental decks following the specifications of Queensland maritime infrastructure were designed, manufactured, and tested to assess the reliability of the new construction system under static flexural loading in the flatwise and edgewise orientations. One segmental deck served as a reference with hand-tight post-tensioning, while the remaining specimens were connected by the GFRP rods with varying levels of post-tensioning. All decks were tested up to failure, allowing for an investigation of their flexural strength, load-strain behaviour, joint opening, and failure mechanism. The results showed that post-tensioning the GFRP rods improves the flexural performance of the segmental decks. The higher the level of post-tensioning, the higher the contact area between the segments at the joint is achieved. A numerical model was developed to understand the detailed mechanism of both flatwise and edgewise specimens. A strain reduction coefficient in the segmental concrete deck under flexure is introduced accounting for the joint presence to reliably calculate the stress in the post-tensioned internal GFRP rod when the concrete in the joint crushes. The system investigated can increase maritime and recreational infrastructure's construction efficiency and provide creative solutions in the GFRP-reinforced concrete structures in the building and construction industry.

1. Introduction

Steel corrosion in reinforced concrete structures presents a significant economic challenge costing around 4 % of a developed nation's gross domestic product [1]. In Australia, out-of-service, maintenance, and replacement activities for steel-corroded infrastructure cost the economy over AU$13 billion annually [2]. The Maritime Safety Queensland division of the Queensland Department of Transport and Main Roads in Australia allocates a minimum of AU$ 10 million annually to keep boating and maritime facilities [3]. Similarly, the Victorian and Australian governments have jointly committed AU$ 50 million to support the maintenance of the infrastructures on Great Ocean Road, a vital tourist route in Victoria that spans 240 kilometres and connects several key towns and coastal villages [4]. There is, therefore, a

significant benefit in using non-corrosive and high-strength reinforcements such as glass fibre-reinforced polymer (GFRP) composite bars to achieve a cost-effective and low-maintenance concrete infrastructure especially those built near coastal and other harsh environmental conditions.

The use of GFRP bars as internal reinforcement, as opposed to traditional steel bars, has been successfully demonstrated in the construction and design of various concrete structures. Examples include pontoon decks [5,6], boating ramp planks and approach slabs [3,7], bridge barriers [8], concrete bridges [9], bridge foundations [10], marine docks [11], piles [12–14], seawalls [15], and concrete slabs [16]. Despite these advancements, many structures in coastal areas and aggressive environments worldwide have not yet benefited fully from the distinct advantages of GFRP bars/rods such as the high strength-to-weight ratio, non-corrosiveness and the ability to be

---

Nomenclature

A_f	Area of the FRP reinforcement.
b	Deck's width.
d	Deck's depth.
d_p	Rod's depth.
E_f	Modulus of elasticity of FRP.
f_c'	Compressive strength of concrete.
f_f	Rod's stress.
f_{fu}	Rod's stress at the failure.
f_{fe}	Effective prestressing stress.
L	Span of the beam.
β_1	Concrete strength factor.
ε_{cu}	Ultimate concrete strain at the extreme compression fibre.
ρ_f	Reinforcement ratio.
ρ_{fb}	Balanced reinforcement ratio.
Ω_u	Strain reduction factor.

prestressed, which provide an opportunity for further optimisation in design. Therefore, ongoing research and development in a newer application are crucial for the widespread use and acceptance of advanced composite reinforcing technologies in maritime concrete structures.

A recent example that can benefit from the continuous improvement in the GFRP-reinforced concrete technologies is the onshore structures. Many of these infrastructures were damaged during the 2022 Queensland flood, which incurred a substantial cost of $7.7 billion [17]. It was also noted that the damage occurred to many critical but steel-corroding maritime infrastructures including pontoon decks. Pontoons or floating walkways are widely used in boating as a launching support and retrieval of recreational trailer boats. It was observed that the damage to these infrastructures is localised but still necessitates the replacement of the entire structure (Fig. 1). A promising solution to this challenge is to manufacture the large precast concrete pontoon into several smaller segments, reinforce the concrete decks internally and connect with GFRP reinforcements. Several studies have highlighted that using GFRP rods as internal post-tensioning systems can effectively address the second-order effect [18,19] and minimise the harping effect [20]. The second-order effect is characterised by a reduction in the effective depth of external prestressed tendons along the deflection of the whole system. In contrast, the harping effect is induced by deviators, leading to stress concentration on the tendons. Moreover, the segmental precast pontoon deck can offer ease of repair [21], improve construction speed [22], facilitate transportation of components, and eliminate the

environmental problems and disturbance associated with in-situ concrete casting processes [23–26]. Furthermore, incorporating the GFRP rod for prestressing can prevent the issue of steel tendon corrosion and eliminate the need for pipe grouting or epoxy in the joint [20,24,27]. A detailed understanding of the structural performance of this new construction system is therefore necessary for its effective and safe design.

Several studies have evaluated the effectiveness of fibre composite rods [28–30] as internal reinforcement in prestressed monolithic concrete beams. The efficiency of the post-tensioned precast segmental system using steel reinforcements was also evaluated by several researchers in T-shaped beams [21,31], box girders [32], and I-shaped cross sections [33]. However, evaluation of the flexural performance of precast segmental concrete beams reinforced by FRP reinforcements is limited. Le et al. [27] comparatively evaluated the performance of carbon fibre-reinforced polymer (CFRP) and steel reinforcements in T-shaped segmental concrete beams. They found that beams with CFRP reinforcements demonstrated excellent load-carrying capacity due to their lighter weight and higher tensile strength than steel. Furthermore, numerical modelling of both internal [22] and external [26] CFRP reinforcements in segmental T-shaped concrete beams showed comparable strength and deformability as steel reinforcements. This demonstrates the high feasibility of using FRP composites as internal reinforcement and prestressing to segmental concrete decks.

Several parameters affect the flexural behaviour of the post-tensioned segmental concrete deck. These parameters include the rod's material [21,27], rod's location within the [22,26], reinforcement ratio [31,34], post-tension type (internal/external) [31], level of initial prestressing [34], loading condition [31], interlocking / joint type [22, 26,33], unbounded length-to-rod's depth [21], concrete strength [18, 25], and the number of segments [34]. For GFRP-reinforced precast segmental decks potentially used in marine infrastructure with a modular manufacturing approach, adjusting the initial post-tensioning is easier to achieve in mass production and can be increased after assembly (using a wrench / hydraulic jack).

Pontoon decks experience various types of loading conditions during their service life. The dead and live loads caused by the self-weight and the expected weight of the people cause the deck to bend along its flatwise direction. In the same way, the decks experience bending in the edgewise direction because of the wave actions and from raging waters during a flooding event (Fig. 2). Consequently, this study aimed to evaluate the effect of the level of post-tensioning force on the flexural behaviour of GFRP-reinforced segmental concrete decks in both the flatwise and edgewise directions. Six large-scale segmental decks were prepared and tested under four-point bending, and their load and deflection behaviour, joint opening, strain responses, and failure mechanisms were thoroughly investigated. A numerical model was developed and an analytical evaluation of the load-carrying capacity of the decks was also implemented. The outcomes of this study will

(a) Near the pile

(b) Between the decks

Fig. 1. Localised damage on the pontoon deck during the 2022 Queensland flood.
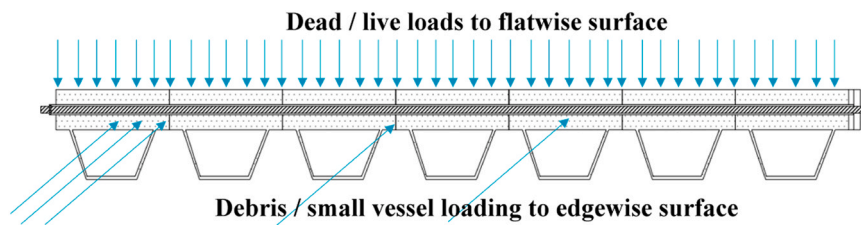
Fig. 2. Different loading scenarios on the segmental pontoon deck.

enhance the construction efficiency of infrastructure for maritime and recreational activities and offer innovative solutions in the field of GFRP-reinforced concrete structures in building and construction.

2. Experimental programme

2.1. Design criteria

The design and manufacturing of the precast concrete segments for the segmental deck adhered to the design criteria outlined by the Queensland Department of Transport and Main Roads [35,36]. More details of the design criteria related to DTMR 2015 [35] have been provided by [6]. The additional technical specification DTMR 2019 [36] offers guidelines for precast concrete members with a design life exceeding 50 years.

2.2. Material characteristics

2.2.1. Concrete

The concrete employed in this study was prepared following the specifications outlined in the MRTS70 [37] guidelines. This mix design of S50 complies with the Australian Standards AS3600 [38] for concrete structures categorised under exposure classification C2 or structures located close to seawater with a minimum cementitious content of 470 kg/m^3 and a maximum water/cementitious ratio of 0.36. More detailed information on the mix design can be found in the previous works [5,6]. Twelve cylindrical specimens were prepared and tested to determine the concrete's compressive strength (f_c'). Each specimen had a nominal diameter of 100 mm and a height of 200 mm, and these tests adhered to the procedures detailed in AS1012.9 [39]. The compressive test results in an average concrete compressive strength of 37.1 MPa, with a standard deviation of 6.2 MPa.

2.2.2. GFRP rebar

The precast concrete pontoon segments were internally reinforced with Grade III (#4) GFRP bars which were manufactured according to CSA S807 [40] and ASTM D7205 [41] specifications. These bars had a nominal diameter of 12.7 mm and were made from longitudinal EC-R glass fibre yarns infused with vinyl-ester resin. A sand coating was added to the bar surface to enhance its bond with concrete. Engineering characteristics of the GFRP bars were assessed by AlAjarmeh et al. [42] and are reported in Table 1.

2.2.3. GFRP rod and end anchorage

Threaded GFRP bars, specifically referred to as rods within the scope of this study, were manufactured by FiReP China Ltd. in Shanghai, China and were supplied by Master Builder Solution-Bluey Company in Australia. These rods were manufactured in full compliance with the specifications outlined in CSA S807 [40]. The fibre content ratio of the rods was 81.9 % determined following the test procedures in ASTM D2584 [43]. The tensile properties of the GFRP rods were evaluated by the University of Sherbrooke and are reported in Table 2. The rod's end anchorage system utilised a threaded stainless-steel tube. This tube had a length of 150 mm, with inner and outer diameters measuring 25 mm and 37 mm, respectively. To facilitate the connection of segments and the application of post-tensioning force, a steel nut with a 38 mm inner diameter was employed. The square steel plate, measuring 100 mm in dimension and 20 mm in thickness, was positioned between the steel tube and the concrete surface (Fig. 4b). This placement aimed to mitigate stress concentration in the concrete region surrounding the rod and steel nut.

The low stiffness of the GFRP flexural members has been one of the primary concerns limiting their applications [44]; therefore, applying post-tensioning is one possible solution to compensate for this concern. The ACI 440.4R-04 [45] recommends designing the FRP reinforcements in concrete structures by limiting the prestressing level to 40 % of the ultimate tensile strength of the reinforcement. Moreover, a methodology's most important part is introducing new technology and its applicability to real-world settings [46–49]. Accordingly, the applied prestressing level mustn't cause a shearing of the rod surface in the steel tube. In this study, the level of post-tensioning is applied based on the maximum shear strength between the GFRP rod and the stainless-steel tube within the anchorage system as reported in Table 2.

Uniaxial testing was then conducted between two rods connected by a stainless-steel coupler in the middle (Fig. 3a). A total of five specimens were tested up to failure. The anchor's average strength of 328.1 kN (equivalent to 756.8 MPa or 56 % of the ultimate tensile strength of the rod) with a standard deviation of 9.4 kN has been achieved. The observed failure was shearing off at the surface threads of the rods (Fig. 3b).

Table 1
GFRP rebar properties and test methods [42].

Internal GFRP		
Mechanical properties	Test method	Value
Nominal diameter (mm)	CSA S807-19	12.7
Nominal area (mm^2)	CSA S807-19	129
Tensile strength (MPa)	ASTM D7205-11	1315
Modulus of Elasticity (GPa)	ASTM D7205-11	62.5
Ultimate strain (%)	ASTM D7205-11	2.3

Table 2
GFRP rod and anchorage properties.

GFRP rods		
Property	Test method	Value
Nominal diameter (mm)	CSA S807-19	23.5
Cross-sectional area (mm^2)	CSA S807-19	416
Tensile strength (MPa)	CSA S807-19	1340
Modulus of Elasticity (GPa)	CSA S807-19	65
Ultimate strain (%)	CSA S807-19	2
Fibre content (%)	ASTM D2584-18	81.9
End anchorage		
Property	Value	Standard deviation
Maximum tensile load (kN)	328.1	9.4
Tensile strength (MPa)	756.8	21.6
Ultimate strain (%)	0.86	0.07

(a) Axial test setup

(b) Failure in anchor

Fig. 3. Tensile testing of the anchorage.

2.3. Specimens detail

Each segment of the deck was designed and manufactured to have dimensions of 1000 mm in length, 600 mm in width, and 125 mm in thickness. The width of the pontoon was determined by the dimensional specifications outlined in [35], which accounts for both the floating and structural components of the pontoon. Subsequently, the thickness of the structural portion was established at 125 mm. The 1000 mm length of each pontoon module was determined by dividing the typical modular length employed in current pontoon manufacturing practices. The transverse GFRP reinforcements were spaced at 2.5 times the plank thickness, which equated to 250 mm, while the longitudinal bar spacing was set at 150 mm on centres (Fig. 4a). This configuration resulted in a transverse and longitudinal tensile reinforcement ratio of 0.82 % and 1.37 %, respectively. The longitudinal reinforcement ratio (Eq. 1) and the balanced reinforcement ratio (Eq. 2) for each segment, following the guidelines in ACI 440.1 R-15 [50], have been calculated (0.21 %).

$$\rho_f = \frac{A_f}{bd} \tag{1}$$

$$\rho_{fb} = 0.85\beta_1 \frac{f'_c}{f_{fu}} \times \frac{E_f \varepsilon_{cu}}{E_f \varepsilon_{cu} + f_{fu}} \tag{2}$$

Following ACI 440.4R-04 [45], the balanced reinforcement ratio of the prestressed segmental concrete beam can be calculated using (Eq. 3), resulting in a value in the range of 0.18 to 0.21 %. Considering the rod for the segmental deck, the reinforcement ratio (ρ_p) is 2.2 % in flatwise and 0.66 % in edgewise orientation (using Eq. 1). This highlights that the segmental deck and each segment are over-reinforced, and the failure is expected to be governed by concrete crushing.

$$\rho_{fb} = 0.85\beta_1 \frac{f'_c}{f_{fu}} \times \frac{\varepsilon_{cu}}{\varepsilon_{cu} + \varepsilon_{fu} - \varepsilon_{fe}} \tag{3}$$

It should be mentioned, in Eq. 3 that ε_{fe} is the effective strain in the rod by the initial prestressing of the segmental deck. In both equations (Eqs.2–3), the maximum compressive strain in the concrete, ε_{cu} is considered 0.003. Six large-scale segmental concrete decks were constructed, each consisting of three assembled and tested segments. Using a wrench, the post-tensioning force was applied by passing the rod through the segments and securing it by tightening the steel nut onto the steel tube (Fig. 4b). To accommodate the GFRP rod, two PVC pipes with
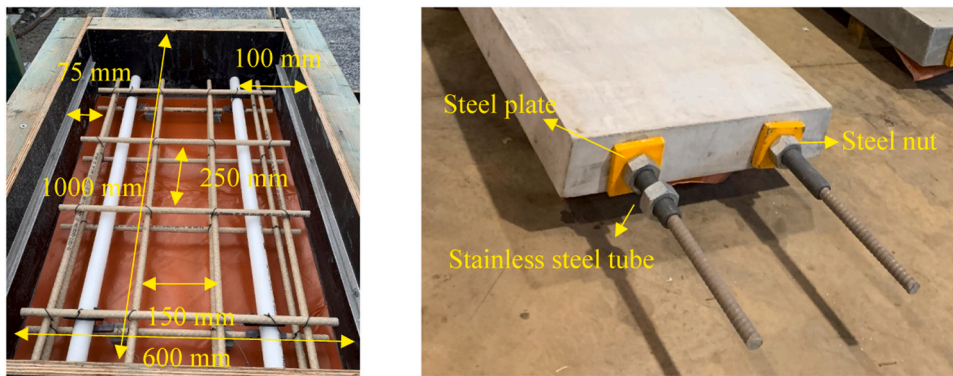
(a) Internal reinforcement

(b) End anchorage

Fig. 4. Deck's details.

a 27 mm inner diameter were positioned in each segment, spaced 400 mm apart or 100 mm from either side of the deck (Fig. 4a). The naming procedure for the deck specimens reflects their loading orientation, with "E" for edgewise and "F" for flatwise, followed by a number indicating the level of applied prestressing force (kN), as measured by the load cell during post-tensioning (Table 3). It should be noted that the maximum level of post-tension force applied in the rod is lower in the edgewise than in the flatwise orientation because of the difficulty and safety of applying the prestressing force in this position.

2.4. Test setup and instrumentation

The segmental decks were tested under a four-point static loading as shown in Fig. 5. The load was applied through a spreader steel I-beam utilising a 2000 kN Enerpac hydraulic jack and measured using a 2000 kN load cell. 3 mm thick rubber matting was placed beneath the loading steel plate to ensure an even distribution of the load to the segmental decks. A digital image correlation (DIC) system was used to track and evaluate deformation patterns along the length of the segmental deck during loading. Strain measurements for the GFRP rods were conducted using 3 mm-long electrical-resistance strain gauges, which were positioned at mid-span and in 50 mm proximity to the deck's support. In the edgewise orientation, the strain gauges were attached to the top and bottom surfaces of the rods. A similar type of strain gauge was attached to the surface of the internal GFRP reinforcement, which was placed at both the bottom and top layers to measure tensile and compression strains. The applied load, prestressing load on the rods, and strains were recorded using the data acquisition system Vishay System 5000.

3. Test result and discussion

Table 4 summarises the observed load-deflection behaviour (also shown in Fig. 6), load-strain relationship, and failure mechanisms. The load-deflection behaviour of the segmental decks, including the cracking load (F_{cr}), ultimate load (F_u) and their corresponding moment, load at 10 mm deflection ($F_{10\,mm}$) and 20 mm deflection ($F_{20\,mm}$) were analyzed to investigate the load-carrying capacity and initial stiffness (k_{el}) and the degraded secondary stiffness in the post crack stage (k_{sec}). The deflection measurements included the sag due to self-weight (δ_{sw}), the deflection at the cracking load (δ_{cr}), and the ultimate load (δ_u). Moreover, the ultimate failure mechanism of each specimen has been identified as premature concrete crushing in the joint (PCC), crushing of the concrete that penetrated the decks' depth (CC), tensile crack propagation in the concrete (TC), and tensile cracks in the GFRP rod (TGR).

3.1. Comparative evaluation of the behaviour between flatwise and edgewise bending

3.1.1. Bending stress and deformation behaviour

The comparison of the effective bending stress and deformation behaviour between the flatwise and edgewise orientations was analysed by assessing the results of the decks F0 and E0 under hand-tight post-tensioning forces. This approach aimed to isolate the impact of post-

tensioning and normalising the behaviour based on their geometrical properties. Normalising the applied load was achieved by considering both decks to have a homogenous cross-section. The effective bending stress at mid-span is calculated as ($\sigma_b = Mc/I$) where M is the applied bending moment, c is the mid-depth of the section, and I is the uncracked second moment of inertia. Moreover, the span-to-depth ratio for E0 and F0 was 1.8 and 8.8, respectively. Generally, a span-to-depth ratio lower than 2.5 beam is typically categorised as a deep beam [51].

Unlike monolithic concrete beams, where linear elastic and nonlinear stages characterised the behaviour, the bending stress and deflection behaviour of flatwise and edgewise-tested decks is primarily governed by the linear-elastic behaviour of the GFRP rod (Fig. 7). The initial stages are influenced by the joint opening at the bottom of the rod and the subsequent closure of the joint at the top. This mechanism results in compression at the top portion of the joint and concrete crushing. As anticipated, due to the higher moment of inertia (2,250,000,000 mm^4 compared to 97,656,250 mm^4) and rod arrangement of edgewise compared to flatwise, the initial stiffness of E0 is higher than that of F0 in the pre-crack stage. While both decks shared an identical cross-sectional area, the effective depth of the rod in the F0 is 87.5 % lower than that in the E0. This reduction significantly diminishes the flexural rigidity of the F0, leading to a pronounced decrease in initial stiffness. The increased effect of the arch action in the edgewise specimens by increasing the effective depth indicated that the beam became more rigid. The lower flexural rigidity of the F0 results in higher vertical deflection under the same level of bending stress. The vertical deflection is correlated with a joint opening in both specimens. The stress between the segments before the opening of the joint is uniformly distributed. However, the opening of the joint in F0 results in the compressive stress concentrating on the top part of the joint causing a concrete crushing. A similar behaviour regarding the influence of depth on bending stiffness has been observed in monolithic GFRP-reinforced concrete beams [52, 53], steel-reinforced segmental concrete beams [21,25], and CFRP reinforcement [26]. These researchers explained that an increase in depth causes an increase in both the gross and effective moments of inertia. When the concrete is not cracking, the increased depth contributes to a higher resistance against deformation. Moreover, as the depth of a section increases, the distance of the extreme fibres from the neutral axis also increases. This results in a larger moment arm, leading to a higher ultimate bending moment and, consequently, greater stiffness. Accordingly, the stiffness in the pre-and post-crack stages was improved by increasing the depth of the section.

Owing to the greater depth and having two rods in different depths instead of both at mid-depth, the self-weight deflection of E0 (4.87 mm) is 70 % lower than F0 (16.35 mm) (Figs. 7 and 8).

Accounting for the deflection of the decks from both the applied load and self-weight, the joint opening in F0 occurred at an equivalent bending stress of 0.67 MPa (1.9 kN), accompanied by a deflection of 16.85 mm. The joint opening in E0 was observed under a bending stress of 0.8 MPa (11.5 kN), with a deflection of 5.97 mm. The difference between the deflections in the crack initiation is attributed to the reduced flexural rigidity of the flatwise orientation, resulting in a higher degree of joint opening and deflection at the same level of effective bending stress.

Table 3
Specimens detail.

Specimen	Width (mm)	Depth (mm)	Location of the rod in tension from the top fibre (mm)	Post-tensioning force (kN)	Equivalent stress (MPa)	Ratio to rod's tensile strength (%)	Ratio to anchor's capacity (%)
F0	600	125	62.5	Hand tight	-	-	-
F10.5	600	125	62.5	10.5	24.2	1.8	3.2
F64	600	125	62.5	64	147.6	11	19.5
E0	125	600	500	Hand tight	-	-	-
E21	125	600	500	21	48.5	3.7	6.4
E45	125	600	500	45	103.8	7.8	13.7

(a) Schematic view

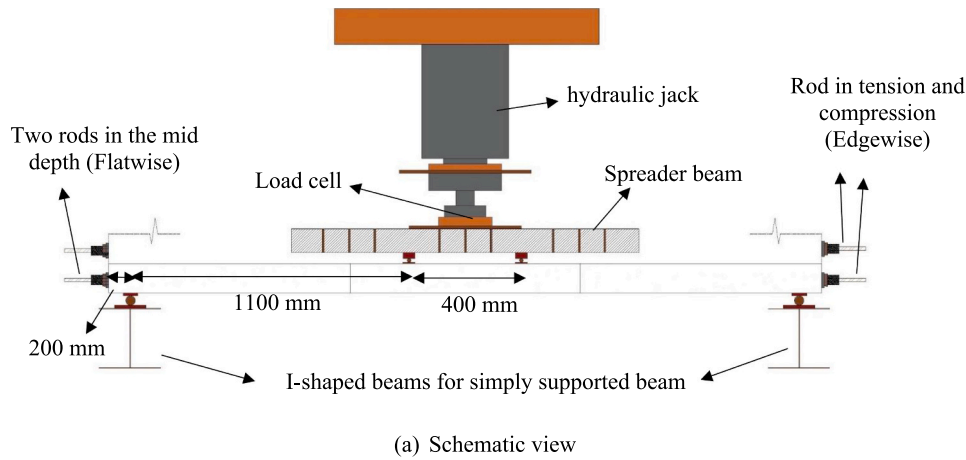(b) Setup for flatwise test

(c) Setup for edgewise test

Fig. 5. Test setup and instrumentation.

With the continuous application of the load, the joint opens and the bending stiffness of the decks decreases. A reduction of 42 % in the flatwise orientation is noted while only an 18 % reduction is measured in the edgewise orientation. This behaviour can be attributed to the higher moment of inertia and increased GFRP rod depth resulting from a change in the deck's orientation. Placing rods at depths of 100 mm (top) and 500 mm (bottom) for the edgewise deck promotes better structural integrity compared to having two rods at the mid-depth (62.5 mm) for the flatwise deck. The average bending stress at failure for the F0 was 8.94 MPa, while that in the E0 was 9.6 MPa. As anticipated, the maximum bending stress in the flatwise specimen is only 7 % lower than the edgewise orientation. This can be explained by the failure of both decks due to the compressive crushing of the concrete at the top portion of the joint. Although the ultimate bending stress in both samples is equal, the ultimate load of F0 (25.4 kN) is 81 % lower than that of E0 (131.3 kN), a result heavily influenced by the 95 % reduction in the moment of inertia from edgewise to flatwise orientation.

The results suggest that segmental concrete decks' maximum capacity is directly proportional to the effective depth; when the depth decreased by 80 %, the ultimate load-carrying capacity reduced by 84 %. It was calculated that the ratio between the bending moment ($\frac{M_{F0}}{M_{E0}}$) and applied loads ($\frac{F_{F0}}{F_{E0}}$) is proportional to the ($\frac{\sigma_{b_{F0}}}{\sigma_{b_{E0}}} \times \frac{h}{b}$). In this relation, σ_b is the bending stress of the specimen, h is the total height, and b is the width of the section. Consequently, since the bending stress of the ultimate stage has a ratio of 0.92, the ratio between the ultimate loads is equal to (0.185), which is nearly equal to the achieved ratio from the experimental results (0.19). In the post-failure behaviour, deck E0 exhibited a 27 mm residual displacement (equivalent to L/1000), while deck F0 showed a 44 mm residual displacement (L/500). This 38 % reduction in residual displacement indicates a better self-centreing capacity in the edgewise loading configuration.

3.1.2. Strain behaviour

Fig. 9 shows the strain behaviour of the GFRP rod under tension (GRTC) and compression (GRCC) at the mid-span and the internal GFRP bars in the corner segment and on the top layer (IRC). It is to be noted that the internal GFRP bars in the segmental deck are not continuous at the joints. This resulted in the internal reinforcement experiencing a low level of strain (in both cases less than 150 μɛ), similar to those reported in previous works [20,54]. On the other hand, the GFRP rods connecting the segments took on the stress, increasing the strain. At the same level of bending stress, a significantly higher strain (and subsequently stress) is measured in the rod in the flatwise (GRTC-F0) compared to the edgewise orientation (GRTC-E0). Under the same deflection (30 mm), the strain on the flatwise orientation reaches 750 μɛ (equivalent to 3.6 % at the ultimate of the rod and 6.3 % of the anchorage). In contrast, the strain in the edgewise orientation is only 170 μɛ, indicating minimal stress on the rod. This observation suggests that the rod in flatwise orientation compensates for the lower moment of inertia by experiencing a higher stress level.

The bending stress-strain behaviour in the rod under compression (GRCC) linearly increases until 0.8 MPa, which is associated with the cracking bending stress. The strain then increases nonlinearly, indicating crack propagation in the compression zone of the joint between segments. Under a bending stress of 1.4 MPa, the strain in the rod under compression reaches − 354 μɛ, nearly ten times higher than the strain in the tensioned rod. In contrast, the strain on the internal reinforcement of the corner segment and near the joint (IRC) exhibits a linear elastic increase up to the ultimate bending stress (9.6 MPa). This behaviour indicates that the crack did not propagate in the corner segment. However, the compression between the segments in the joint caused the stress to be concentrated in the middle segments between the joint and the loading point. This observation aligns with the failure behaviour observed in the test. The strain magnitude, in the same level of bending

Table 4
Summary of the results.

| Specimen	F_{cr} (kN)	M_{cr} (kN.m)	$F_{10\,mm}$ (kN)	$F_{20\,mm}$ (kN)	F_u (kN)	M_u (kN.m)	K_{el} (kN/mm)	K_{sec} (kN/mm)	$(F_{rod}^+)_{max}$ (kN)	$(F_{rod})_{max}$ (kN)	δ_{sw} (mm)	δ_{cr} (mm)	δ_u (mm)	Failure mode
F0	1.9	1.05	2.62	5.36	25.43	13.98	0.28	0.16	96.3	-	16.35	6.8	136.1	PCC
F10.5	5.4	2.98	4.03	6.62	27.37	15.05	0.3	0.22	106.78	-	4.19	12.5	156.21	PCC
F64	8.93	4.91	14.98	16.13	17.8	9.8	7.08	4.15	138.03	-	2.08	1.26	43.45	CC + TGR
E0	11.5	6.35	29.59	66.95	131.32	72.26	6.18	5.07	170.89	-0.55	4.87	1.86	63	CC+TC
E21	28.73	15.8	44.23	103.44	167.52	92.13	6.69	5.83	191.5	-0.2	0.1	0.7	75.44	CC+TC
E45	53.15	29.23	90.5	153.1	185.5	102.2	14.7	8.31	194.7	3.7	0.03	3.42	60.8	CC+TC
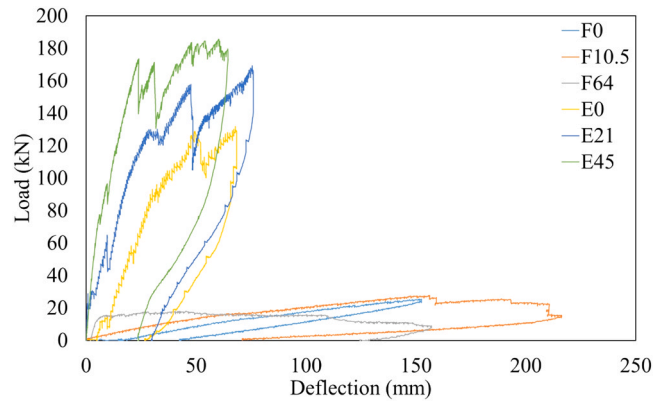
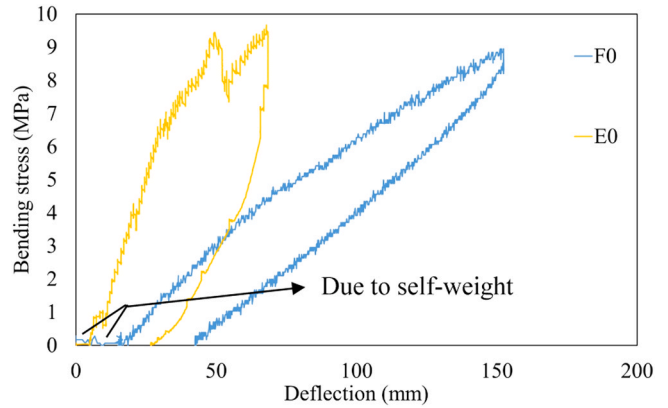

Fig. 6. Load-deflection curves.

Fig. 7. Effect of the deck orientation on the bending stress-deflection behaviour.

stress, for top internal reinforcement (IRC) and bottom rod (GRTC) for the edgewise deck is nearly identical, suggesting strain compatibility across the depth of the section until a bending stress of approximately 7.0 MPa. This marks the onset of concrete compression crushing at the top joint (Fig. 10) for the decks tested in both flatwise and edgewise orientations. This concrete crushing decreased the bending stiffness of the decks and the cracks propagated in the corner segments in the tension zone.

3.1.3. Failure mechanism

Both flatwise and edgewise decks failed at an effective bending stress of around 7 MPa. The observed failure mechanism involved progressive concrete crushing in the joint and at the compression zone of the middle segment near the loading point. Beyond this bending stress level, the concrete crushing at the flatwise-oriented deck is significantly progressing. In contrast, the edgewise-oriented deck exhibited a deeper crack in the compression zone and symmetrical concrete cracking in the corner segments in the tension zone (Fig. 11), attributed to the tensile stress created by the deflected bottom rod. Moreover, the higher moment of inertia of the edgewise deck resulted in an increased resistance against joint opening, leading to a higher depth of concrete in compression. Therefore, the angle of the crack between the loading point and the joint was 14.5 degrees in the flatwise orientation, whereas it was 37 degrees in the edgewise orientation (Fig. 11). This observation agrees with [27] that increasing the depth of the prefabricated concrete beam's internal reinforcement increases the plastic hinge's depth (compressive concrete region from the joint to the loading point). The described behaviour is crucial because the ability of the segmental system to resist vertical deflection relies on the contact area between the
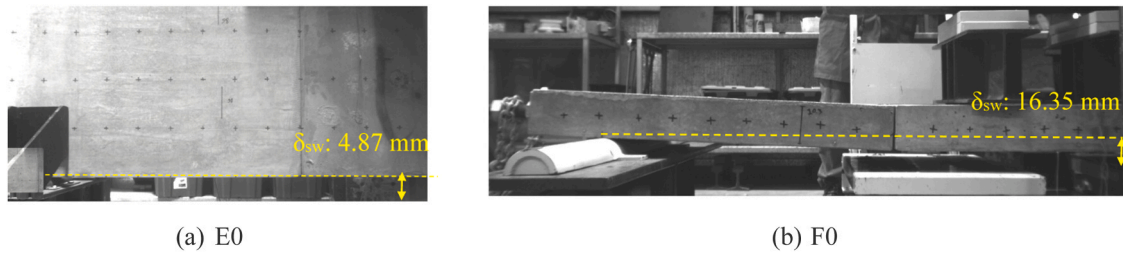
(a) E0   (b) F0

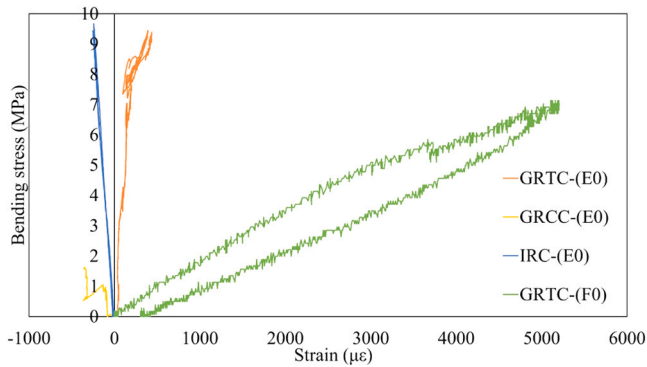**Fig. 8.** Captured self-weight deflection by DIC.

Fig. 9. Effect of the deck orientation on the load-strain behaviour.

joints at the interface of the segments. A larger compression depth results in greater resistance, leading to higher bending stiffness and, consequently, increased bending capacity.

The observed failure behaviour of the segmental pontoon decks is in contrast with that of the indicated failure mode in AASHTO-2003 [55] which suggested that the failure will be governed by the tension control mode when c/d < 0.42, where c is the depth of the neutral axis and d is the distance from the extreme top fibre. According to ACI 440.4R-04 [45] for FRP prestressed concrete beam, the c/d ratio can be calculated from $\frac{\varepsilon_{cu}}{\varepsilon_{cu}+\varepsilon_{fu}-\varepsilon_{fe}}$, which is equal to 0.25 in the current system. In the design criteria from AASHTO [55], the steel reinforcements are assumed to be yielded and the concrete is crushed, which is similar to the failure behaviour reported by [18,27]. This suggests that the conventional specifications for segmental concrete members might not be appropriate for the segmental system with an unbonded GFRP rod. This is attributed to the linear elastic behaviour of the FRP, the level of applied prestressing force and the system's reliance on the concrete in compression at the joint.

3.2. Effect of level of post-tensioning on flatwise bending

3.2.1. Load-deflection behaviour
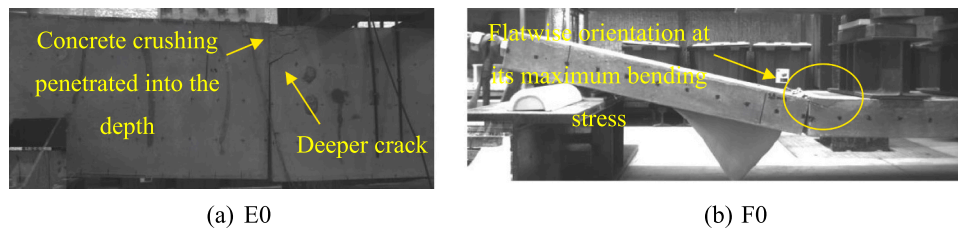Increasing the level of post-tension in the GFRP rod decreases the

(a) E0   (b) F0

Fig. 10. Crack formation at bending stress equal to 7 MPa.
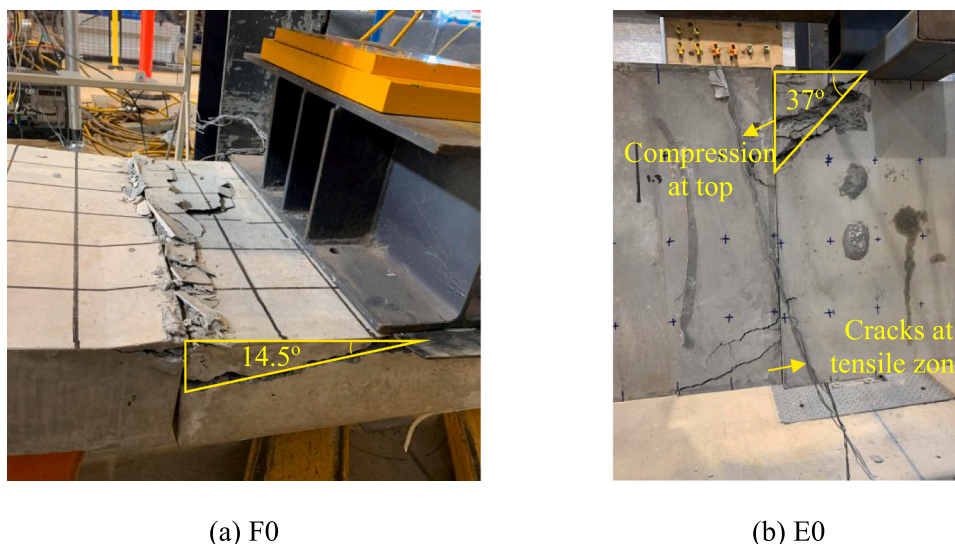

(a) F0   (b) E0

Fig. 11. Effect of the deck orientation on the failure behaviour.

deflection of the deck due to its self-weight. From a midspan deflection of 16.3 mm for hand-tight, this decreases to 4.2 mm for F10.5 (74 % reduction) and 2.1 mm for F64 (87 % reduction). The reduction in the deflection is due to the higher friction caused by the interface of the segments. When the joint at the bottom opened, the concrete at the top of the joint started to be crushed (Fig. 12).

Based on the equilibrium equation in the section, the depth of the neutral axis can be calculated using Eq. 4. Also, the moment capacity M_{cc} when the concrete crushes can be determined with Eq. 5, where a is the depth of the equivalent compression block and is equal to ($\beta_1 c$).

$$c = \frac{2A_f\left(f_f + f_{fe}\right)}{0.85f'_c b\beta_1} \tag{4}$$

$$M_{cc} = 2A_f f_f\left(d - \frac{a}{2}\right) \tag{5}$$

In Eqs. 4 and 5, d is 62.5 mm, β_1 is calculated from the equation in ACI 440.1 R-15 [50] and is equal to 0.78, b is equal to 600 mm, and the f'_c is 37.1 MPa. The tensile force provided by the GFRP rods ($A_f f_{fe}$) is assumed to be equal to the applied post-tensioning load. The load on the rod ($A_f f_f$) for each specimen is assumed to be the value of the load when the concrete is crushed (61, 66, 74 kN for F0, F10.5, and F64, respectively). These values were obtained from the load at which concrete reached its maximum strain for F64 (Fig. 15), which is also correlated with the corresponding deflection (Fig. 14a-b). These load levels are very close to the values at which the concrete is crushed in the joint. Accordingly, the depth of the neutral axis is determined to be 10.6 mm, 11.0 mm, and 19.8 mm, and the moment capacity is equal to 7.1, 7.7, and 8.1 kN.m for F0, F10.5, and F64, respectively. This shows that increasing the level of post-tension causes a higher depth of the neutral axis, resulting in a bigger area of compression block between the segments in the joint (Fig. 17). These values are close to the experimental results (Table 5), and on average, have a 15 % difference which can be attributed to the standard deviation of the measured concrete compressive strength of 6.2 MPa (16 % of f'_c). Fig. 13 shows the deviation of the calculated neutral axis depth with the range of the measured compressive strength of the concrete. The illustration in Fig. 13 suggests that the calculated depth of the neutral axis (Eqs. 4 and 6), used in equations for bending capacity (Eqs. 5 and 7), is based on the average compressive strength of the concrete. However, due to the standard deviation, the neutral axis depth for each specimen has a range, and the reported value is an average.

Before the joint opens, i.e., midspan deflection of lower than 3 mm, a non-linear correlation was observed between the initial post-tension force and the initial bending stiffness, approximating a relationship proportional to $(P_{fe})^{1.8}$, where P_{fe} denotes the effective horizontal load force generated by the initial post-tensioning.

The relationship of the axial load measured in the rod and the midspan deflection behaviour of the decks in Fig. 14b showed a linear elastic behaviour before concrete crushing regardless of the level of post-tensioning. A similar observation was made by [20,27]. Before the joint opening (2-mm deflection) the increment in the axial load is the same in all samples. As concrete crushing initiates, the lower slope in the rod's load increment shows up (non-linear stage). This is attributed to the fact that when the concrete passes the elastic limit and is crushed in

Table 5
Experimental versus theoretical values.

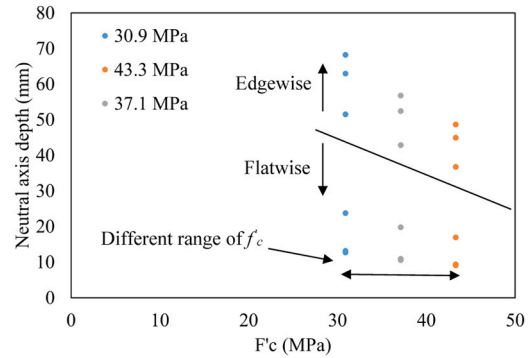| Specimen	Neutral axis depth (mm)	M_{exp} (kN.m)	$M_{Theoretical}$ (kN.m)	Error (%)
F0	10.6	5.7	7.1	19.7
F10.5	10.98	6.9	7.7	10.3
F64	19.8	9.6	8.1	15.6
E0	42.9	71.11	63.8	10.2
E21	52.44	85.9	71.6	16.6
E45	56.8	94.2	83.1	11.7

Fig. 13. Variation of the neutral axis depth with compressive strength of concrete.

the top part of the joint the contact area is removed or reduced. Decks with higher post-tension (F64) levels exhibited a more distinct nonlinear behaviour. This can be attributed to the larger area of the concrete crushing in compression.

Regardless of the level of post-tensioning, an increase in deflection leads to an increase in axial load as the rod experiences higher deflection due to bending and the loadcells in the end anchor measure a higher load. A comparison between the load-deflection and rod's load increment-deflection in F10.5 reveals that, despite the increase in axial load due to bending, the load-deflection curve exhibits a reduction in load-carrying capacity. Therefore, it is more accurate to examine the behaviour of axial load before concrete crushing and any development of cracks in the compression part, which can induce a non-linear behaviour in the axial load-deflection curve. In this stage, there is a contact area in the interface of the joint but gradually decreases due to the progressive crack propagation.

3.2.2. Strain behaviour

The load-strain response of the internal GFRP reinforcement in the middle concrete deck segment located near the joint's compression zone (IRC) of F64 is linear until a load of 17.8 kN (Fig. 15). With the continuous application of the load, a sudden rise in strain up to -2600 $\mu\epsilon$ which led to the concrete crushing at the joint. Rods in F0 endure higher strain but experience higher strain because of the higher deflection, resulting in higher curvature of the deck and, therefore, more stretching of the rod at the same level of load. Consequently, the strain in the rod and the mid-span (GRTC) at the same load level (10 kN) reveals
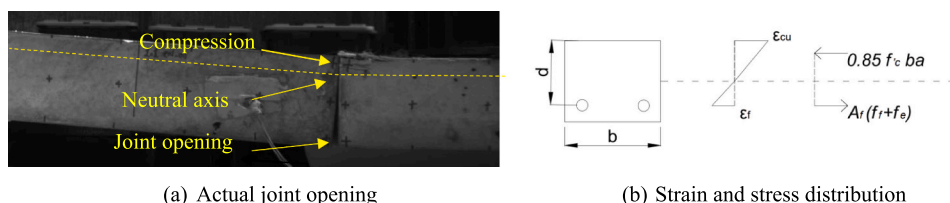

(a) Actual joint opening

(b) Strain and stress distribution

Fig. 12. The section at the joint opening.

(a) Applied load-deflection
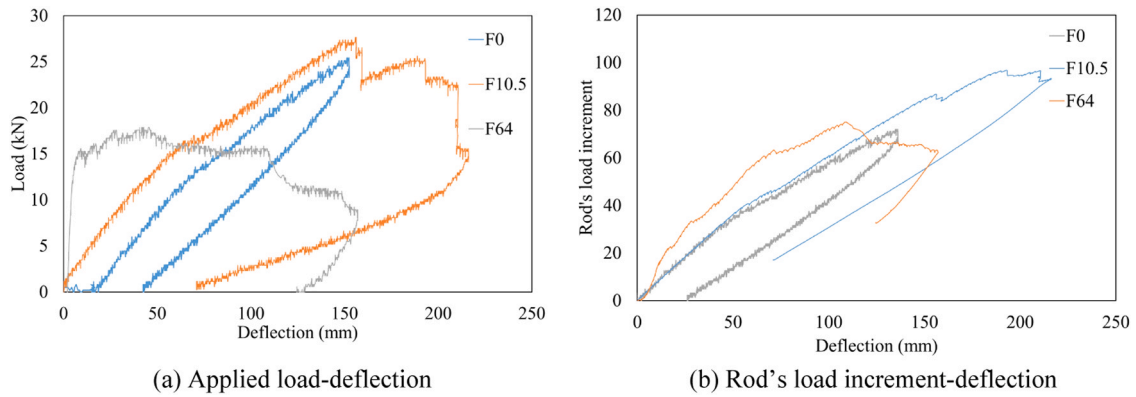

(b) Rod's load increment-deflection

Fig. 14. Effect of the post-tension in the load-carrying capacity of the flatwise orientation.

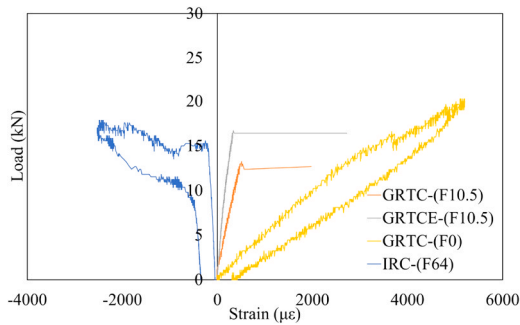**Fig. 15.** Applied load-strain in flatwise orientations.

that the hand-tight rod endures higher strain (1946 με) compared to F10.5 (346 με). A comparison between GRTC and GRTCE shows that due to higher deflection, strain (and hence stress) in the mid-span is higher than in the location near the support. This behaviour aligns with observations in segmental slab post-tensioned by steel reinforcements, where the reinforcement near the support exhibited an elastic phase while the mid-span experienced plastic deformation [18].

3.2.3. Failure behaviour

The opening of the bottom portion of the joint resulted in the crushing of the concrete at the top portion of the joint. Fig. 16 shows the joint opening of decks F0 and F10.5 follows the same trend but with the joint starting to open at an applied load of 5 kN. The width of the joint opening continues to increase with the application of the load. In contrast, the joint in F64 only opens at an applied of 15 kN. After this load, however, the joint opening becomes wider even without any significant increase in the applied load. This result suggests that the joint opening can be minimised by applying a high level of prestressing to the GFRP rods. Moreover, the rotation and deflection of the deck will be
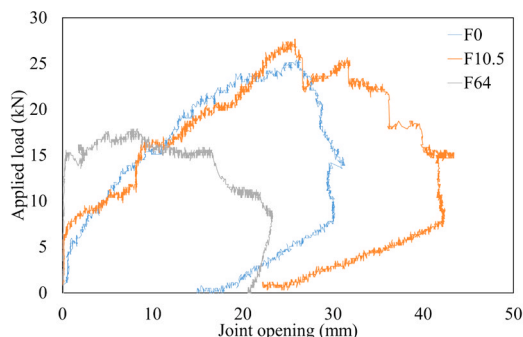

Fig. 16. Applied load-joint opening (flatwise).

minimised until the concrete in the joint fails in compression.

The results showed that a higher initial post-tension led to a greater similarity from a segmental to a monolithic structure, the same as the segmental slab prestressed by steel reinforcement [21,31,32]. By comparing the F64 and F10.5 (and hand-tight specimen) it is evident, that after the joint opening, post-tensioning alone no longer singularly regulates the joint's behaviour. Another significant effect of post-tensioning is an increase in the compression depth in the joint, from 8.9 mm in the F0 to 18 mm in the F64 (Fig. 17). This observation can be explained by the larger area of concrete in compression to resist the higher tensile force in the GFRP rod. This behaviour is analogous to a monolithic beam, where an increase in the initial level of prestressing leads to an increase in the depth of the neutral axis. In the segmental deck, this translates to an increased depth of the compression block between the segments.

3.3. Effect of the post-tensioning on edgewise orientation

3.3.1. Load-deflection behaviour

Fig. 18 shows the load-carrying capacity of the edgewise decks. The results show that applying the post-tensioning (2.14 times) in the edgewise configuration enhances the bending stiffness by 2.2 times before cracking and 1.75 times after cracking (Fig. 18a). Higher post-tensioning equates to a deeper neutral axis, which causes a larger area of the concrete to be in contact with each other in the joint, distributing the compressive force over a larger area. This causes a segmental deck to tolerate a higher load in the same level of deflection which causes an increase in stiffness and load corresponding to the joint opening as well. This was predicted and also similar ratio in observed by [21,24] by increasing the post-tension by 1.22 times the bending strength improved by 1.3 times. In the post-crack stage, despite crack propagation in the compression zone, the post-crack stiffness improved by 42 % as the post-tension force increased from 21 to 45 kN. When the top part of the joint near the cracks experiences compression due to bending and from the initial post-tensioning load of the unbonded rods, the cracks close (or are prevented from propagation), and the segmental deck behaves similarly to an intact beam. This phenomenon is similar to the flexural crack development observed in post-tensioned monolithic beams [56].

The ultimate load-carrying capacity of E45 was 10 % higher than that of E21, indicating that ultimate load capacity is improved by post-tensioning force. This is due to segments maintaining contact with each other, and the area of concrete in compression increases which minimises any stress concentration at the top of the joint. This behaviour is observed in other studies [20,21,24], however, it is associated with a reduction in specimen ductility, as predicted and observed by [18,20,21, 24,25].

The increment-deflection curve for the bottom rod (Fig. 18b) showed a slight increase in the pre-crack stage, starting before joint opening (up to 1 mm deflection), a pattern similar to what was observed by Hu et al.
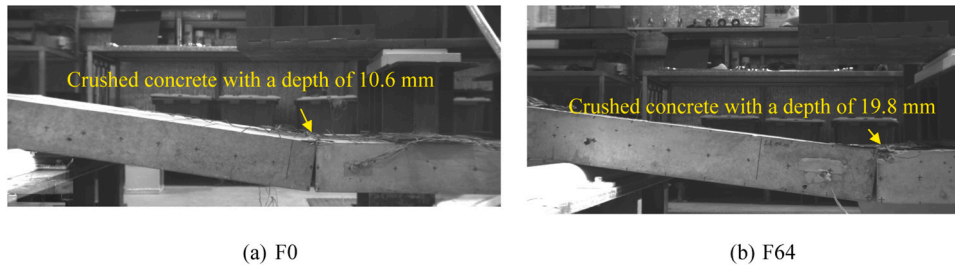
(a) F0   (b) F64

Fig. 17. Effect of the post-tensioning on the failure behaviour.

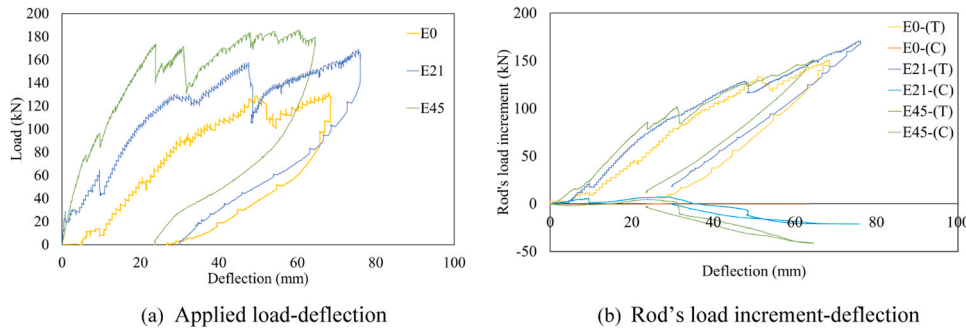(a) Applied load-deflection   (b) Rod's load increment-deflection

Fig. 18. Load-carrying capacity in edgewise decks.

[25]. Following this, in the post-crack stage (joint opening), a more significant increase was evident, and the rod's increment exhibited a higher increase in post-tensioned samples during crack propagation (up to 30 mm deflection). Nevertheless, as the loading (and deflection) increases and the joint undergoes progressive crushing, the contact area between the segments decreases, causing a reduction in the deviation between the increments. Consequently, after 32 mm of deflection, the increment in all specimens becomes similar. This stage of crack propagation and concrete crushing corresponds to changes in the load in the rod under compression (in E21 and E45), indicating complete crushing of the concrete, the crack due to compression reaching the rod, and the top rod being exposed to compression.

The neutral axis depth of the segmental decks tested in the flatwise direction can be calculated using Eq. 6. At the same time, the ultimate moment of concrete crushing can be determined using Eq. 7, as follows:

$$c = \frac{A_f \left(f_{ft} + 2f_{fe} - f_{fc} \right)}{0.85 f_c' b \beta_1} \tag{6}$$

$$M_{cc} = A_f \left(f_{ft} \left(500 - \frac{\beta_1 c}{2} \right) + f_{fe} \left(600 - \beta_1 c \right) + f_{fc} \left(\frac{\beta_1 c}{2} - 100 \right) \right) \tag{7}$$

In these equations, the contribution of the prestressed GFRP rods in the compression zone is also considered. Here $(A_f f_{ft})$, $(A_f f_{fc})$, and $(A_f f_{fe})$ are the forces provided by the GFRP rods in tension, compression and initial post-tension load, respectively. Table 5 lists the values of each parameter presented in Eqs. 4 to 7. It should be mentioned the bending moment $M_{Theoretical}$ in these equations is the calculated value when the concrete in the top part of the joint is crushed. The theoretical values are derived from an assumed f_c' of 37.1 MPa, and the experimental results show an acceptable level of accuracy when compared to the theoretical values when considering the average f_c' in the calculations.

3.3.2. Strain behaviour

Fig. 19 presents the relationship between the applied load and strain in the GFRP rods. Up to 28 kN, there is almost no strain recorded in GRTC (E0 and E21) indicating that the joint is still closed, no cracks have emerged, and the contribution of the rod is minimal. During this stage,

which aligns with the closure of the joint, the segmental deck primarily depends on the compression between segments. Beyond 28 kN, and in the post-crack stage, the load-strain profiles diverged, while the rod's strain in E0 did not measure any stress, in E21, it significantly contributed to the load-carrying capacity. Accordingly, at the same loading level (120 kN), the strain in E21 reached 3791 µε compared to E0, which only reached 430 µε. This indicates. This is anticipated and suggests that the initial prestressing involves the internal GFRP rod in the load-carrying capacity. Simply placing the rod without the initial tensile prestressing load does not notably enhance the flexural behaviour. The strain on the internal reinforcement (IRT) in tension (bottom layer) exhibited a negligible increase. Theoretically, due to the joint cut-off, there is no contribution of longitudinal reinforcement in the tension zone of the section which agrees with the test results.

3.3.3. Failure behaviour

The applied load-joint opening behaviour in the edgewise orientation reveals four distinct stages (Fig. 20).

Stage I is characterised by the pre-crack stage exhibits a steep slope (Fig. 21a). Stage II is characterised by initial crack propagation, marked by a plateau phase (Fig. 21b). Increasing post-tension improves both stages by raising the cracking load and reducing the plateau part or limiting joint opening due to initial cracks. Stage III signifies a non-
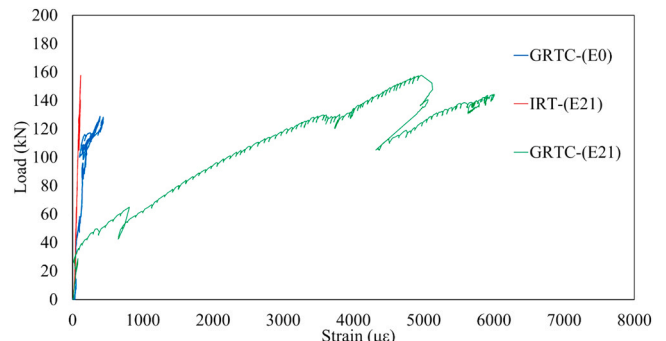

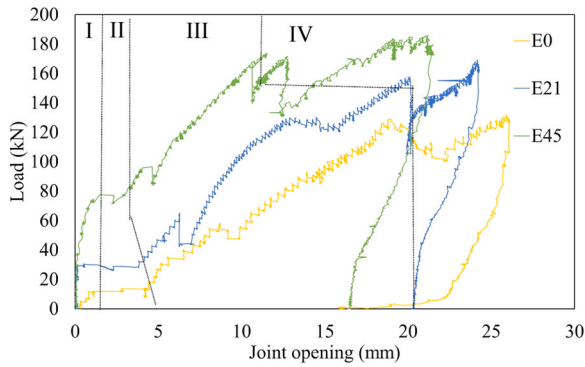**Fig. 19.** Applied load-strain in edgewise orientation.

Fig. 20. Applied load-joint opening in edgewise orientation.

linear phase linked to stiffness degradation and initiation of the crack penetration (Fig. 21c). Enhanced post-tensioning improves performance by mitigating stiffness degradation, although at the expense of reduced ductility in the segmental deck. Stage IV represents the post-concrete crushing response after the drop (Fig. 21d). In this stage, while the load-carrying capacity of E0 did not increase, E45, due to the presence of horizontal force on the segmental deck, provided the ability to bear more loading. Comparing the applied load-deflection and applied load-joint opening curves in the edgewise orientation emphasises the correlation between them. In the load-deflection diagram, when a drop occurs (indicating the development of a crack), in the load-joint opening, a plateau phase becomes evident, suggesting that concrete is crushing on the top part of the joint. In contrast, the opening occurs in the bottom part of the joint.

4. Numerical analysis

4.1. General description

The experimental results were numerically verified using Abaqus/

CAE [57] by developing a three-dimensional model of the segmental decks and employing a dynamic explicit solver to simulate the response under four-point loading. The choice of a dynamic explicit solver was based on its efficiency compared to a standard solver, making it suitable for handling larger and more complex models. The numerical analysis was conducted using the displacement-controlled method to replicate the experimental conditions. Moreover, the deflection due to the self-weight of the concrete deck is excluded in the numerical verification and the external loading is considered. The results from numerical evaluation support the experimental findings and help establish an analytical assessment.

4.2. Constitutive relations of material

4.2.1. Concrete

In the numerical analysis, the precast concrete segments were modelled using C3D8R solid elements as this element type is well-suited for simulating the behaviour of solid structures, including concrete. The determination of the compression depth in flatwise orientation, which ranges between 10.6 and 19.8 mm, requires a smaller mesh size. However, reducing the mesh size significantly increases computation time without a substantial impact on the load-carrying capacity, as tried in the sensitivity analysis. Therefore, a 12.5 mm mesh size for the solid element was chosen. However, for the edgewise orientation, a 20 mm mesh size is considered sufficient to identify the compression depth between the segments with acceptable accuracy.

Table 6 shows the concrete properties used in simulation. The elastic properties, such as the elastic modulus, were calculated as $E_c = 4700\sqrt{f'_c}$ following the ACI 318–08 [58]. Poisson's ratio (υ) was set to 0.18, a value commonly adopted in previous studies for concrete materials such as [21]. The plastic damage model of concrete (CDP) was employed for the non-linear stage of concrete behaviour which also considers the stiffness degradation and the development of cracks. The plastic parameters, including flow potential eccentricity, viscosity parameter, and the second stress variation, were derived from the studies by Tran et al.

(a) Stage 1

F_{E0}:

7.5

F_{E21}:

28

F_{E45}:

37

(b) Stage 2

F_{E0}:

13

F_{E21}:

30

F_{E45}:

72

(c) Stage 3

F_{E0}:

126

F_{E21}:

154

F_{E45}:

169

(d) Stage 4

F_{E0}:
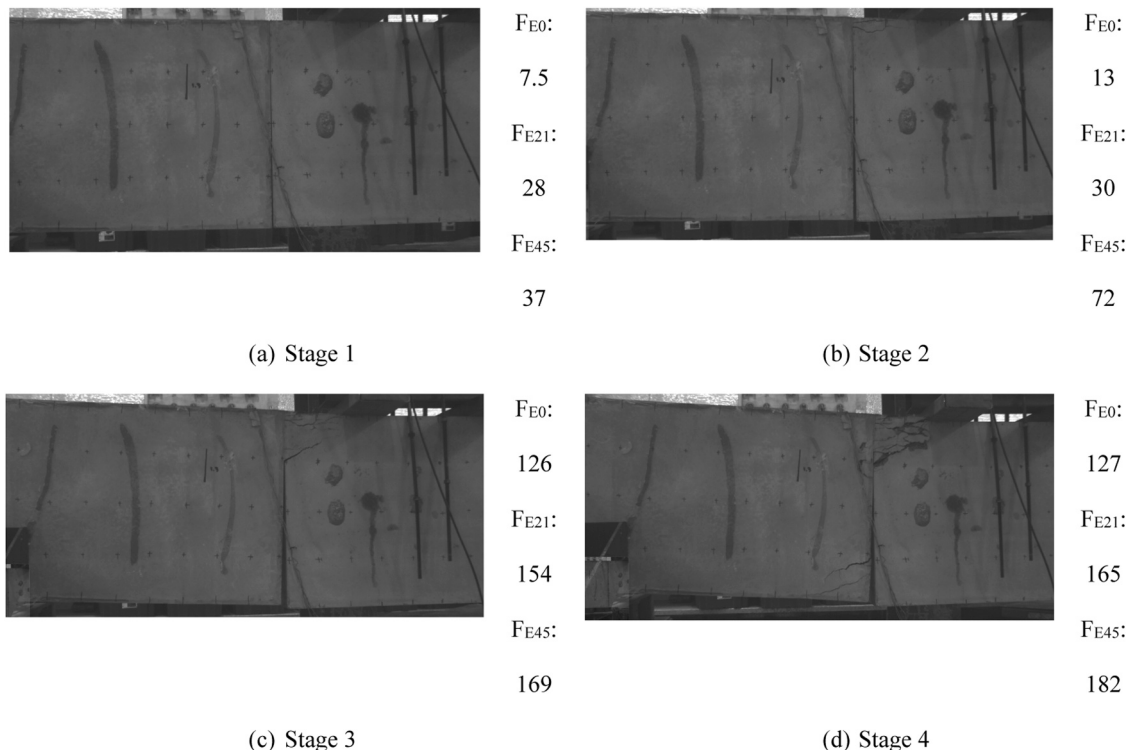
127

F_{E21}:

165

F_{E45}:

182

Fig. 21. Failure mechanism in edgewise orientation.

Table 6

Properties of concrete.

General and elastic properties		Plasticity properties	
Density (Ton/mm^3)	2.64e-09	Dilation angle (ψ)	33
Elastic modulus (MPa)	28,600	Eccentricity	0.1
Poisson's ratio	0.18	f_{b0}/f_{c0}	1.144
		K_c	0.6667
		Viscosity	0.001

[22,26]. These parameters were chosen based on the similarity in the compressive strength of the concrete used in both studies. The ratio of initial equi-biaxial compressive yield to initial uniaxial compressive yield stress ($\frac{\sigma_{b0}}{\sigma_{c0}}$) was calculated using the equation ($\frac{\sigma_{b0}}{\sigma_{c0}} = 1.5(f'_c)^{-0.075}$) suggested by Papanikolaou & Kappos [59] and determined to be 1.144.

The compressive behaviour of the concrete was modelled based on the approach proposed by Carreira & Chu [60], as follows:

$$\sigma_c = \left(\frac{\beta\left(\frac{\varepsilon_c}{\varepsilon_0}\right)}{\beta - 1 + \left(\frac{\varepsilon_c}{\varepsilon_0}\right)^\beta}\right) f'_c \tag{8}$$

$$\varepsilon_0 = \left(168 + 0.71 f'_c\right) 10^{-5} \tag{9}$$

where β is the material factor that depends on the stress and strain relationship and can be calculated as:

$$\left(\frac{0.4 f'_c}{E_c \varepsilon'_c}\right)^\beta - \beta \times \left(\frac{f'_c}{E_c \varepsilon'_c} - 1\right) - 1 = 0 \tag{10}$$

In the numerical model, the elastic stage under compression is assumed until the compressive stress surpasses 40 % of the concrete's compressive strength. This implies that the concrete exhibits elastic behaviour until the applied compressive stress reaches a specific threshold. Once this threshold is exceeded, the concrete transitions into nonlinear behaviour, incorporating compression hardening. The elastic stage under tension concludes when the tensile stress reaches the tensile strength of concrete extracted from equation ($f_{ct} = 0.33\sqrt{f'_c}$) adopted from AS3600–2018 [38]. Accordingly, the behaviour of the concrete can be demonstrated in Fig. 22a. The damage parameters of the CDP model were adopted from the equations that have been employed in different previous studies [21,22,26].

$$d_c = 1 - \left(\frac{\sigma_c}{f_c}\right) \tag{11}$$

$$d_t = 1 - \left(\frac{\sigma_t}{f_t}\right) \tag{12}$$

4.2.2. GFRP reinforcements

In the numerical model, the internal GFRP reinforcing bars and rods were represented using solid elements with a mesh size of 10 mm (C3D8R), providing a realistic simulation of rebar. The elastic modulus of the internal GFRP rebar (62.5 GPa) was determined based on (Table 1). An orthotropic behaviour (via Engineering Constants in Abaqus) for the internal GFRP rod has been adopted. While the longitudinal tensile strength and longitudinal modulus were extracted directly from (Table 2), major and minor Poisson's ratios were adopted from [61]. The other parameters of the orthotropic material including, transverse tensile strength, modulus, in-plane shear strength, and shear modulus were adopted from [62] due to the close fibre content ratio to the GFRP rod in the current study. Table 7 shows the GFRP propoerties used in simulating rebars and rods.
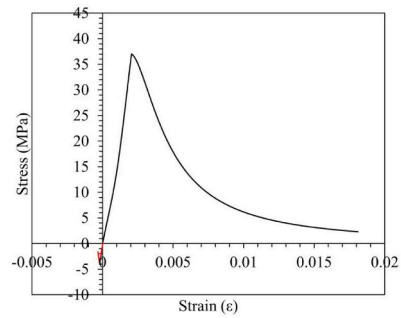
(a) Concrete behaviour
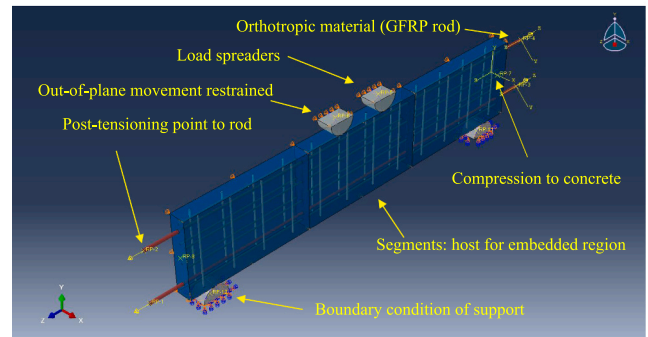
(b) Assembled specimen (edgewise)

Fig. 22. FE model Details.

4.3. Boundary conditions

The "Embedded region constraint" was employed (Fig. 22b) to model the interaction between the internal GFRP bars and concrete. This constraint simulates the embedding and confinement of the GFRP rebars within the segment, treating it as a "host region." It ensures that the internal GFRP bars stay embedded within the concrete and do not separate. Throughout the loading process in the numerical model, "tie constraints" were used to connect load spreaders to reference points on the middle segment. This facilitated the application of a monotonic displacement to the plank, replicating the loading conditions observed in the experimental tests. Employing normal "hard contact" behaviour and tangential behaviour based on the "Penalty" option and with a friction coefficient of 0.8 is appropriate for simulating the interaction between elements. This coefficient was adopted from the sensitivity analyses varying the value from 0.3 [63] to lower than 0.9 [21,22,26], which is within the typical friction coefficient of the concrete surface between 0.5 and 0.9 [64]. This assumption is a friction coefficient to replicate the roughness of the surfaces and the resulting resistance to sliding.

In the numerical model, the application of initial post-tension to the specimens was simulated by adding four reference points in the centre of

Table 7

GFRP properties.

Rebar		Rod			
Density (Ton/mm^3)	2.2e-09	Density (Ton/mm^3)	2.2e-09		
Young's Modulus (MPa)	62,500	E1 (MPa)	65,000	υ_{12}	0.06
Poisson's ratio	0.28	E2 (MPa)	8600	υ_{13}	0.06
		E3 (MPa)	8600	υ_{23}	0.28
		G12 (MPa)	3600	G23 (MPa)	3600
		G13 (MPa)	3600		

the GFRP rod. A "tie constraint" was employed to ensure that the tension force was evenly applied to the rods. To simulate the overall post-tensioning process, the reaction (compression force) was applied at the centre of the corner segments, tied to the surface of the concrete. This approach does not consider stress concentration around the steel nut but captures the post-tensioning process. The displacement was applied to the structural deck with a ramp loading rate, and the initial post-tension force was applied instantly from the beginning of the loading protocol. The gap between segments for hand-tight specimens is closed by the application of a 1.5 kN post-tensioning load (150 με) during the test.

4.4. Model verification

The results of the numerical analysis were verified from the experimental results covering the load-carrying capacity, strain behaviour in the GFRP rod and concrete, and the failure behaviour of the concrete in the joint. Throughout the numerical modelling and verification, the strain and failure behaviour in the GFRP rod was evaluated as this information is difficult to measure and observe experimentally. Moreover, the numerical modelling provided additional information to have a detailed behaviour of the concrete at the joint.

4.4.1. Load-carrying capacity

The numerical validation of the load-carrying capacity was conducted up to 70 mm, considering F0 and F64 in flatwise orientation (Fig. 23a) and up to 40 mm for E0 and E45 in edgewise orientation (Fig. 23b). First, F0 was simulated, measuring the load on the bottom surface of the support versus the mid-span deflection. Subsequently, a 64 kN load was applied to the GFRP rod, and the process was repeated. It is worth noting that the experimental load cell during the test was positioned on top and between the actuator and the spreader, meaning that gravity was not measured. Therefore, gravity was not applied to the numerical model.

The comparison for F0 between the finite element analysis (FEA) and experimental results showed a good correlation in the load-carrying behaviour pre- and post-joint opening. Slight differences between the numerical modelling and experimental results could be attributed to variations in the compressive strength of concrete, estimation of the friction coefficient in the model, and potential imperfections in fitting the segments in the large-scale testing compared to the perfect alignment in the model. These factors may cause slight differences in stiffness. However, considering the overall behaviour up to 70 mm, F0-FEA and F0-EXP behaviours were similar.

With the application of the 64 kN load, as predicted, the load associated with joint opening and concrete crushing increased, leading to an increase in the initial elastic stiffness. The cracking loads of F64-FEA (14.36 kN) are closely aligned with the experimental results of F64-EXP (13.8 kN). However, the stiffness of F64-FEA in the non-linear stage, coinciding with the concrete crushing of the joint in the top part, was higher than in the experiment, especially after 30 mm. This

difference could be attributed to noise in the load-carrying behaviour induced by concrete elements failing in the joint and the F64-EXP results were within the range of maximum and minimum values, making the FEA results acceptable. Moreover, the difference could be attributed to the procedure of post-tensioning. In the experimental sample, the GFRP rod is under tension, and the load is transferred to the concrete through the steel plates (not evenly to the section). In the F64-FEA, the compression load is evenly and effectively transferred to the segments in the centre of the cross-section throughout the test, causing a higher non-linear load-carrying behaviour.

Rotating the flatwise model and subjecting it to a 40-mm deflection was the method employed to measure the load on the support and assess the load-deflection behaviour. However, the load-carrying capacity in edgewise orientation, the same as the experimental result, exhibited a similar increase in initial stiffness from E0 to E45. However, there were slight discrepancies between the initial stiffness of the FEA and experimental results. This difference can be attributed to the heterogeneity of the concrete material in the experimental sample compared to its homogeneity in the FE model, as also observed and reported by Obaidat et al. [65]. Without post-tensioning, the model precision for E0 was generally good throughout the 40-mm deflection, with a perfect match in behaviour. However, in E45, as observed in F64, there is a discrepancy. While the first 10 mm has a good prediction, from 10–15 mm, the slope in FEA is higher. This difference may be attributed to the same reason observed in F64, namely, a better and more uniform distribution of compression to the section in the experimental sample.

4.4.2. Strain behaviour

The evaluation of the strain behaviour of concrete in joints is crucial, and the element size is 12.5 mm (flatwise specimens), dividing the 125 mm depth into 10 elements. The naming convention for elements uses a number, where the number indicates the number of the element from the top located in the joint. For example, in F64–3, the concrete element in F64, precisely in the joint, is the third element from the top (mid-distance from the top is 31.25 mm). The concrete element's strain behaviour was analysed by the time the displacement through the load spreader was applied. Evaluating the strain in the joint throughout the determined period (1 s) in dynamic explicit analysis helps exclude any noise observed in capturing the load from the support.

F0–1 exhibits a substantial increase in strain as soon as the external load is applied in the experiment, indicating a similar behaviour to premature failure (Fig. 24a). This is attributed to stress concentration in sharp corners observed in numerical modelling (Fig. 25a-c). Additionally, F0–2 shows almost zero strain during the test, suggesting that the neutral axis is located between the first and second elements. While this is close to theoretical calculations (10.6 mm), the numerical model suggests that due to stress concentration, this depth is higher in the sharp corners. In contrast, the strain in F64–1 shows a more gradual increase in loading, indicating more uniform compression between the segments due to the presence of post-tensioning (Fig. 25d). F64–2 initially does not show any increment, but as the joint further opens, it
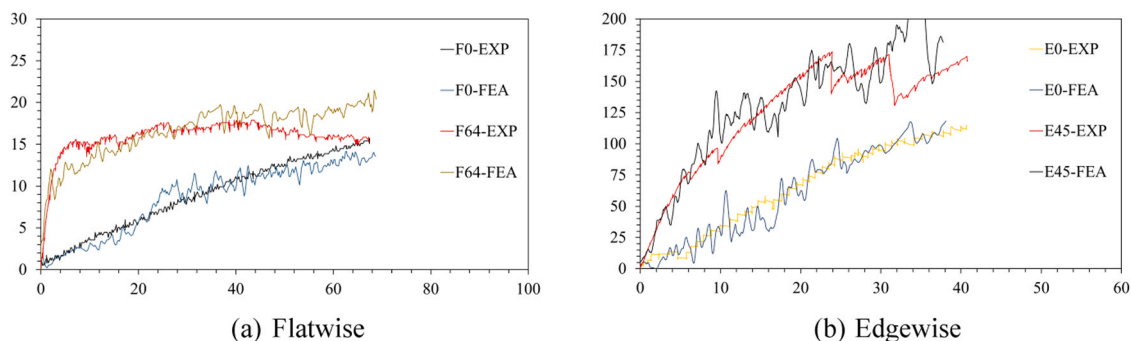
(a) Flatwise

(b) Edgewise

Fig. 23. Load-displacement of FEA vs experiment.

(a) Flatwise

(b) Edgewise
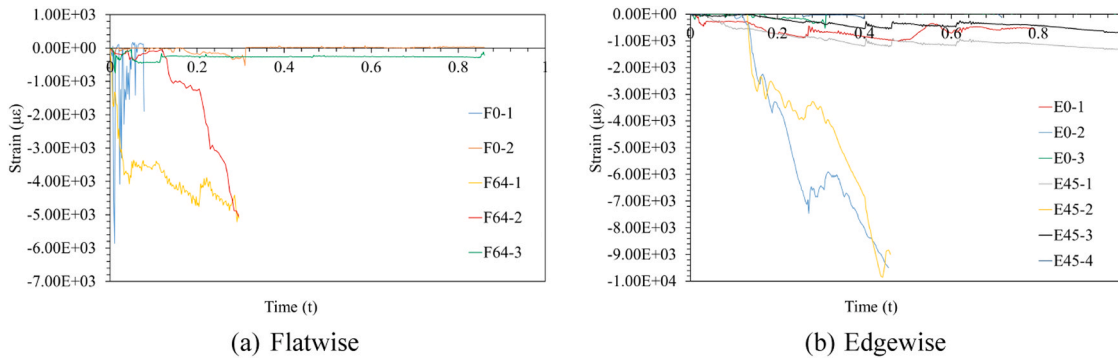
Fig. 24. Strain behaviour of concrete in the joint.

(a) F0 (S_{33} @ 1.1 kN & 3.25 mm)

(b) F0 (DAMAGE @11.2 kN)

(c) Ultimate failure F0

(d) F64 (S_{33} @1.2 kN & 0.4 mm)

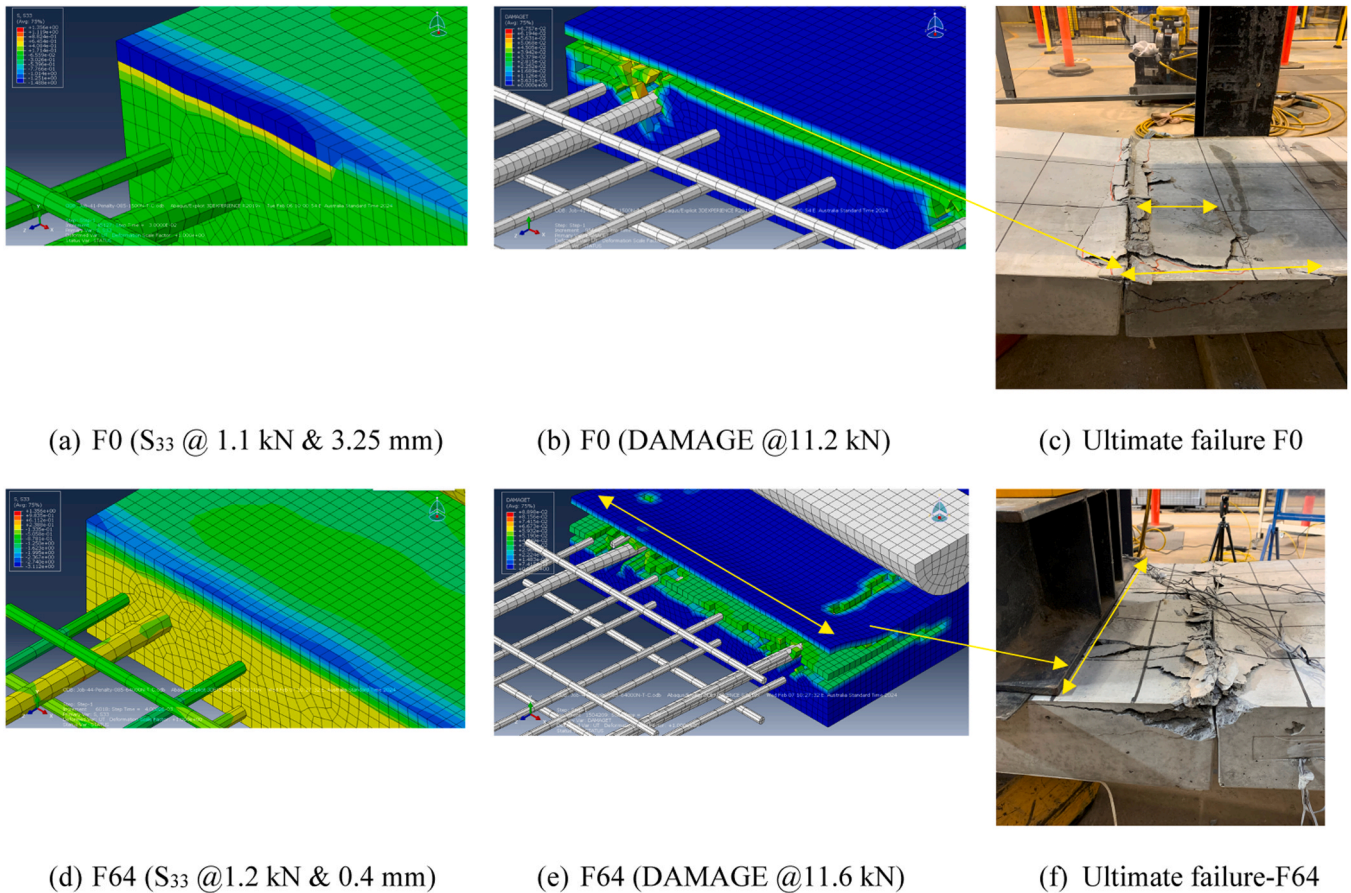(e) F64 (DAMAGE @11.6 kN)

(f) Ultimate failure-F64

Fig. 25. Failure behaviour (Flatwise).

becomes compressed. This indicates that while the joint is open, both elements are under compression. F64–3 does not show any increase, suggesting it is not completely under compression, and the neutral axis is located around 25 mm depth, validating the neutral axis when the concrete crushes based on theoretical calculations (19.8 mm).

In edgewise orientation (Fig. 24b), the highest compressive strain was observed on the second element from the top (20–40 mm), where the damage was initiated in E0 (Fig. 26a) and E45 (Fig. 26b). While the strain of the third concrete element from the top in E0 is completely zero, the similar element in E45 reached almost − 1000 με, suggesting the compression depth even when the crack initiated between 20–40 mm from the top continued somewhere between 40–60 mm from the top. However, the fourth element in E45 has a very similar strain increment to the third element in E0, suggesting this element was

located in the joint opening depth. Accordingly, it can be mentioned the depth of the compression in E0 is located around 40 mm from the top while in E45 is located at 40–60 mm which is close to the theoretical results.

4.4.3. Failure mechanism

The post-tensioning of the GFRP rod leads to an increased depth of compression and a more uniform distribution of the contact area in the joint when the joint is closed (1.1 kN applied load), the bending stress in the section of F0 shows higher stress in the corner and top of the GFRP rod, whereas, in F64, it is distributed along the joint (Fig. 25). Furthermore, the bending stress validates the strain behaviour, as in F0, the top element is just under compression (Fig. 25a), while in F64, the second element is also under compression (Fig. 25d). This stress in the
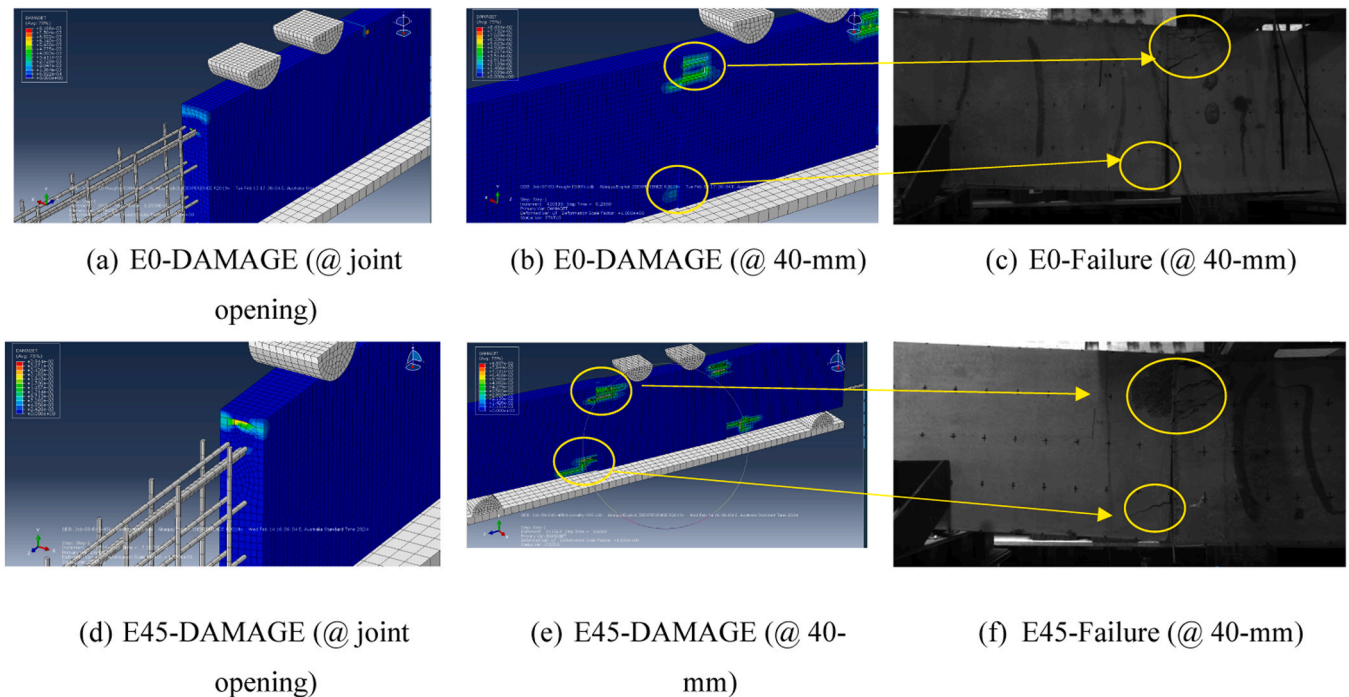
(a) E0-DAMAGE (@ joint opening)

(b) E0-DAMAGE (@ 40-mm)

(c) E0-Failure (@ 40-mm)

(d) E45-DAMAGE (@ joint opening)

(e) E45-DAMAGE (@ 40-mm)

(f) E45-Failure (@ 40-mm)

Fig. 26. Failure behaviour (Edgewise).

joint persists, leading to a failure mechanism focused on the compression zone of the joint in F0 and concentrating on the top corner and interface of the rod and concrete (Fig. 25b); however, the concrete crushing is more developed in the sharp corners of the cross-section (Fig. 25c). In F64 concrete, the whole width of the joint is compressed, with a higher depth (Fig. 25e). This observation indicates the more uniform distribution of the compression between the segments (Fig. 25f).

The comparison of the failure mechanism of E0 and E45 reveals that in the joint opening, the crack in E0 is initiated between the first and second elements, where the whole second element from the top is at the edge of the cracking (Fig. 26a). In E45, this is shifted deeper to the second and third elements. The failure at 40 mm deflection in E0 shows damage due to joint crushing and initiation of damage at the same depth as the tensioned GFRP rod (Fig. 26b-c), while in E45, the crack is already developed at this level (Fig. 26e-f).

5. Analytical evaluation

Prior investigations have demonstrated that traditional prediction codes [66,67] tend to underestimate the load capacity of concrete members with internally prestressed CFRP reinforcements [20]. This underestimation can be attributed to these codes restricting the use of unbonded internal reinforcements in dry joint bridge designs and the assumption is based on the external reinforcements. In the current system, GFRP post-tensioned segmental concrete members with an unbonded internal rod, the failure mechanism is highly dependent on the contact area between the joints, resisting vertical deflection. Hence utilising the equation provided in ACI 440.4 R-04 [45] for concrete members prestressed by FRP, with modification, might offer a more accurate approach [18,22,26,27]. Based on Eqs. 4–7, following force equilibrium in a section, there is a relationship between the bending capacity and the initial prestressing load, and the rod's stress (and consequently axial load) achieved from the experiment. In these equations, the initial pre-stressing stress, rod's cross-section, width, and depth are known and the only parameter that is extracted from the experimental program is the rod's load (stress) when the concrete is crushed. Hence predicting the rod's load can translate to the bending capacity. Based on ACI 440.4 R-04 [45], the rod's stress at the failure in the post-tensioned deck with an unbonded FRP rod is provided (Eq. 13).

$$f_{fu} = f_{fe} + \Omega_u E_p \varepsilon_{cu} \left(\frac{d_p}{c_u} - 1 \right) \tag{13}$$

In (Eq. 13), L, E_p, and ε_{cu} are equal to 2600 mm, 65 GPa, and 0.003, respectively. d_p is taken to be 62.5 mm and 500 mm in flatwise and edgewise orientations. The c_u in the above equation is the neutral axis depth at the ultimate stage, however, as will be discussed in the segmental deck the neutral axis depth, which is provided in Table 5, when the concrete crushes will be used (c_{cc}). Ω_u is the strain reduction coefficient and under the four-point bending and uniform loading test, this value can be taken to be equal to $\frac{5.4}{(L/d_p)}$ as suggested by Naaman [68]. Various studies have put forward different strain reduction coefficients to enhance the accuracy of segmental concrete beams. For instance, Le et al. [21] proposed a coefficient of $\frac{2.4}{(L/d_p)}$, Tran et al. [26] suggested it to be equal to $\frac{0.24}{(L/d_p)^{0.1}}$ while Alkhairi [69] introduced this coefficient as $\frac{3}{(L/d_p)}$. It is worth noting that all studies used a T-shaped cross-section with an unbonded length to the beam's depth ratio of 9. Accordingly, the predicted values based on the different strain reduction factors can be calculated and listed in Table 8. The last column related to the error in this table indicates the accuracy of the proposed reduction factor compared to the experimental results.

The experimental result is the value of the rod's load when the concrete is crushed, hence results reveal an underestimation in the predicted values of the [45,69] for the flatwise orientation, attributed to the presence of the joint causing a concrete crushing at a lower applied load, similar to the results of Tran et al. [26] (Fig. 27 a-b). This can explain why the beam theory is no longer applicable for predicting the concrete stresses after the joint opening as also reported by [32]. Moreover, it is important to note that ACI 440.4 R-04 [45] limits the application of its equations to monolithic beams prestressed with FRP reinforcements with unbonded lengths greater than 15 times the beam's depth. In this study, the ratio between the unbonded length of the rod to the beam's depth was 5.2 and 41.6 for the edgewise and flatwise orientation, respectively. By increasing the post-tension level, the accuracy improved which means the behaviour is similar to a monolithic

Table 8

Experimental versus predicted values.

| Specimen	GFRP Rod's load					
	Experimental	ACI 440.4 R-04[45]	Alkhairi[69]	Tran et al.[26]	Proposed factor	Error (%)
F0	61.1	53.7	29.8	68.4	49.7	18
F10.5	66.3	62.4	39.5	76.5	58.5	11.3
F64	74.2	90.3	79.8	96.8	88.5	19.3
E0	85.8	491.7	273.18	163.3	91.8	7
E21	92.9	415.76	240.7	168.7	95.4	2.7
E45	101.5	407	246.94	181.1	114.1	12.4
Experimental/ predicted value						
Average		0.61	0.96	0.69	0.99	-
Standard deviation		0.41	0.67	0.15	0.13	-
Variance		0.199	0.55	0.028	0.022	-
Confidence Interval (95 %)		0.61 ± 0.32	0.96 ± 0.53	0.69 ± 0.12	0.99 ± 0.1	-
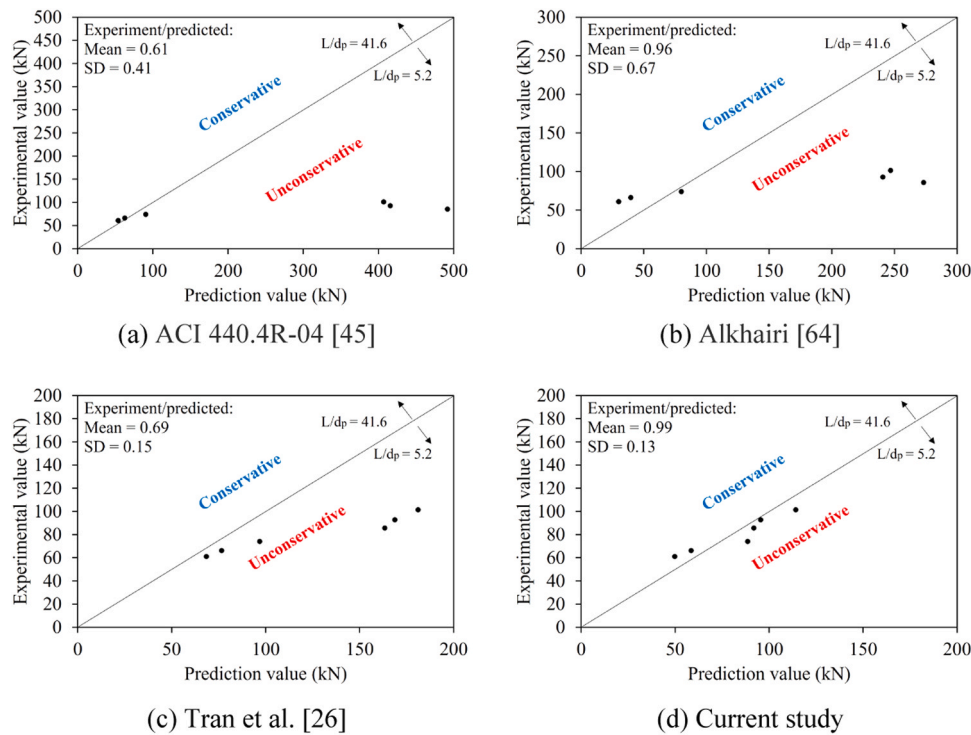
Fig. 27. Accuracy of the prediction equation for different models.

beam which is the basis of the reduction factors. Conversely, in the edgewise orientation, an overestimation is evident using that of ACI 440.4R-04 [45] and Alkhairi [69] but consistent with those of Le et al. [21] and Yan et al. [18]. This indicates that a high overestimation occurs when the unbonded length to the deck's depth ratio is lower than 15. The statistical metrics show that a high standard deviation and variance exist when using the equation of Alkhairi [69] but the average values are close between the ACI 440.4 R-04 [45] and Tran et al. [26]. It is essential to note that the reduction factor proposed by [26], which is exponentially influenced by the length-to-deck depth ratio, demonstrates improved accuracy for both edgewise and flatwise segmental decks (Fig. 27c). However, the reduction factor in both orientations tends to lead to overestimation.

In the current system, due to a lack of bonding between the rod and concrete, the strain compatibility of the rod and surrounding concrete is maintained as long as the concrete is not crushed. The rod stress is transferred to the structure via the end anchorage and Eq. 8 is not applicable to predict the ultimate stress in the rod. However, it can predict the level of stress in the rod at the concrete crushing with some modifications. Consequently, this study proposes a reduction factor for

internal GFRP post-tensioned segmental concrete decks, which is determined based on a formulation of $(0.0994 + 0.0005(L/d_p))$. Accordingly, the prediction equation can be modified following the formulation in (Eq. 14).

$$f_{cc} = f_{fe} + \left(0.0005\left(\frac{L}{d_p}\right) + 0.0994\right)E_p\varepsilon_{cu}\left(\frac{d_p}{c_{cc}} - 1\right) \qquad (14)$$

The introduced strain reduction factor in the formula considers the high compression stress of the segments at the joint in the segmental concrete deck causing concrete crushing to occur earlier than the monolithic beam. Also, in the proposed equation, the increment of the load due to initial pre-stressing is dependent on the depth of the rod and the neutral axis (d_p/c_u). The physical meaning of the coefficient indicates when the concrete joint crushes, 10–13 % of the GFRP rod's tensile capacity has been used and showed better accuracy (Fig. 27d). The proposed coefficient for the prediction equation is more accurate for the experimental results in this study as demonstrated by the mean value of the experimental-to-predicted value of 0.99. Moreover, the results also have low standard deviation and variance providing a high level of

confidence from the obtained results. This behaviour may be limited to the segmental deck prestressed internally with unbonded GFRP rods and under the four-point flexural bending. Further testing and evaluation are suggested to understand the behaviour of this construction system under the effect of other environmental circumstances such as buoyancy, soil interaction, and point loads created by vessels or debris hitting the sides of the deck.

6. Conclusion

This study investigated the flexural response of segmental concrete decks reinforced internally with GFRP rebar and post-tensioned using GFRP rods. Six large-scale specimens with different levels of prestressing force were tested under a four-point bending test in the flatwise and edgewise orientations. The flexural behaviour in terms of load deflection, strain responses, joint opening, and failure mechanisms was evaluated. A FE model was developed to verify the experiment results and an analytical assessment by revising the ACI equation considering a strain reduction factor was developed to reliably describe the moment capacity of the segmental decks. Based on this study, the following conclusions can be drawn:

- The behaviour of hand-tight segmental decks in both flatwise and edgewise orientations is governed by the concrete compressive crushing at the joint. The rate of joint opening and effective bending stress at failure were similar.
- Increasing the level of post-tensioning in the GFRP rod improved the stiffness of the decks in the flatwise specimens. Moreover, a higher friction is developed between the segments at the joint interface enhancing the segmental decks' loading capacity and deformation resistance. Increasing the level of post-tensioning in the rod increased the depth of the compression block resulting in a more progressive compressive crushing of the concrete.
- Post-tensioning of the GFRP rods in concrete decks tested in the edgewise orientation increased the initial stiffness and reduced the opening of the joints. Tensioning the rods minimises the stress concentration at the top of the joint resulting in progressive cracking and increasing the ultimate load capacity of the decks. The decks also failed by a combination of concrete crushing at the top and bottom of the joint.
- By assuming an orthotropic material for GFRP, the nonlinear behaviour of concrete, which is essential for compression behaviour in segmental systems, and appropriate boundary conditions, a numerical model can successfully capture the depth of the compression between the segments at the joint.
- A strain reduction coefficient is introduced to the ACI 440 equation to reliably predict the bending capacity of prestressed GFRP reinforced segmental concrete decks. The coefficient considers the ratio of the deck's depth to the rod's unbonded length. Moreover, the coefficient considers the presence of a joint in the segmental deck causing stress in internal rods when the concrete crushes reach 9.9-15 % of its maximum tensile strength.

The results of this study demonstrated the high potential of the segmental precast concrete decks for a pontoon deck or boat ramp in onshore marine structures. Future research is needed to understand the interaction of the post-tensioned segments with soil/foundation (as a boat ramp) and the behaviour when it is exposed to tidal waves and buoyancy conditions (pontoon). Moreover, it is recommended a parametric study be conducted to optimise the design and to demonstrate the applicability of the experimental results to other loading scenarios as well as the scalability of the segmental deck with a different width dimension and more segments in length.

CRediT authorship contribution statement

Reza Hassanli: Writing – review & editing, Supervision, Methodology. **Brahim Benmokrane:** Writing – review & editing, Supervision, Methodology. **Allan Manalo:** Writing – review & editing, Supervision, Resources, Project administration, Funding acquisition, Conceptualization. **Shahrad Ebrahimzadeh:** Writing – original draft, Methodology, Investigation, Formal analysis, Data curation, Conceptualization. **Charles-Dean Sorbello:** Writing – review & editing, Supervision, Resources, Project administration, Funding acquisition, Conceptualization. **Senarath Weerakoon:** Writing – review & editing, Supervision, Resources, Project administration, Funding acquisition, Conceptualization. **Omar Saleh AlAjarmeh:** Writing – review & editing, Supervision, Methodology, Funding acquisition, Conceptualization. **Xian Yang:** Writing – review & editing, Validation, Methodology, Conceptualization.

Declaration of Competing Interest

The authors would like to declare and confirm that there is no conflict of interest of this manuscript.

Acknowledgements

References

[1] Koch G. Cost of corrosion. Trends oil Gas Corros Res Technol 2017:3–30.
[2] Mohammed AA, Manalo AC, Ferdous W, Zhuge Y, Vijay PV, Alkinani AQ, et al. State-of-the-art of prefabricated FRP composite jackets for structural repair. Eng Sci Technol, Int J 2020;23(5):1244–58.
[3] Manalo A, Alajarmeh O, Yang X, Ferdous W, Ebrahimzadeh S, Benmokrane B, et al. Development and mechanical performance evaluation of a GFRP-reinforced concrete boat-approach slab. Structures 2022;46:73–87.
[4] Mahmoodian, M., Li, C.Q., & Setunge, S. (2015, June). Service life prediction of coastal infrastructures in Australia. In E-Proceedings of the 36th IAHR World Congress, Held During (Vol. 28).
[5] Ebrahimzadeh S, Yang X, Manalo A, Alajarmeh O, Senselova Z, Sorbello CD, et al. Flexural behaviour of GFRP-reinforced concrete pontoon decks under static four-point and uniform loads. Structures, 59. Elsevier,; 2024, 105796.
[6] Yang X, Alajarmeh O, Manalo A, Benmokrane B, Gharineiat Z, Ebrahimzadeh S, et al. Torsional behavior of GFRP-reinforced concrete pontoon decks with and without an edge cutout. Mar Struct 2023;88:103345.
[7] Manalo AC, Alajarmeh O, Cooper D, Sorbello CD, Weerakoon SZ, Benmokrane B. Manufacturing and structural performance of glass-fiber-reinforced precast-concrete boat ramp planks. Structures, Vol. 28. Elsevier,; 2020. p. 37–56.
[8] Benmokrane B, Nazair C, Loranger MA, Manalo A. Field durability study of vinyl-ester–based GFRP rebars in concrete bridge barriers. J Bridge Eng 2018;23(12): 04018094.
[9] Selmy YM, El-Salakawy EF. Behaviour of circular concrete bridge columns internally reinforced with GFRP under reversed-cyclic loading including torsion. Structures, Vol. 59. Elsevier,; 2024, 105680.
[10] Nolan S, Rossini M, Knight C, Nanni A. New directions for reinforced concrete coastal structures. J Infrastruct Preserv Resil 2021;2(1):1–12.
[11] Nolan, S., & Nanni, A. (2023). Marine Dock with FRP Bars and Seawater-Mixed Concrete. In: Proceedings of Italian Concrete Conference 2020/21 (Vol. 351, p. 17). Springer Nature.
[12] Rodriguez R, Benzecry V, Nolan S, Nanni A. Design and driving performance of two GFRP-reinforced concrete piles. Spec Publ 2022;356:152–69.
[13] Benmokrane B, Mohamed HM, Mousa S, Elsafty A, Nolan S. Design, construction, testing, and behavior of driven precast concrete piles reinforced with GFRP bars and spirals. J Bridge Eng 2021;26(8):04021050.
[14] Yang Z, Xu C, Li G. Behavior of GFRP tube confined hollow high-strength concrete short columns under axial compression. Structures, Vol. 61. Elsevier,; 2024, March, 106017.

[15] Steputat C, O'Connor J, Arrants M, Beech J, Nanni A. GFRP-RC seawalls as a means of coastal fortification and extended service life. Concr Int 2022;44(11).

[16] Mostafa HM, Mahmoud AA, Mostafa TS, Khater AN. Experimental and analytical punching shear behavior of reinforced concrete flat slabs having internal GFRP gratings. Structures, Vol. 60. Elsevier,; 2024, 105882.

[17] Queensland Reconstruction Authority. (8 June 2022). The social, financial and economic costs of the 2022 South East Queensland Rainfall and Flooding Event. Available on: ⟨https://www.qra.qld.gov.au/sites/default/files/2022-07/dae_rep ort_-_south_east_queensland_rainfall_and_flooding_event_-_8_june_2022.pdf⟩.

[18] Yan W, Jiang F, Chen L, Sun Y. Proposals for flexural capacity prediction of precast segmental concrete beam prestressed with internal un-bonded CFRP tendons. Appl Sci 2023;13(11):6652.

[19] Peng F, Xue W, Tan Y. Design approach for flexural capacity of prestressed concrete beams with external tendons. J Struct Eng 2018;144(12):04018215.

[20] Le TD, Pham TM, Hao H, Hao Y. Flexural behaviour of precast segmental concrete beams internally prestressed with unbonded CFRP tendons under four-point loading. Eng Struct 2018;168:371–83.

[21] Le TD, Pham TM, Hao H. Numerical study on the flexural performance of precast segmental concrete beams with unbonded internal steel tendons. Constr Build Mater 2020;248:118362.

[22] Tran DT, Pham TM, Hao H, Chen W. Numerical investigation of flexural behaviours of precast segmental concrete beams internally post-tensioned with unbonded FRP tendons under monotonic loading. Eng Struct 2021;249:113341.

[23] Zhu Y, Zhang Y, Shi J. Finite element analysis of flexural behavior of precast segmental UHPC beams with prestressed bolted hybrid joints. Eng Struct 2021;238: 111492.

[24] Yan W, Chen L, Han B, Xie H, Sun Y. Numerical model for flexural analysis of precast segmental concrete beam with internal unbonded CFRP tendons. Materials 2022;15(12):4105.

[25] Hu Z, Xu Z, Zhang S, Jiang H, Chen Y, Xiao J. Experimental study on shear behavior of precast high-strength concrete segmental beams with external tendons and dry joints. Buildings 2022;12(2):134.

[26] Tran DT, Pham TM, Hao H, Chen W. Numerical study on bending response of precast segmental concrete beams externally prestressed with FRP tendons. Eng Struct 2021;241:112423.

[27] Le TD, Pham TM, Hao H, Yuan C. Performance of precast segmental concrete beams posttensioned with carbon fiber-reinforced polymer (CFRP) tendons. Compos Struct 2019;208:56–69.

[28] Grace NF, Abdel-Sayed G. Behavior of externally draped CFRP tendons in prestressed concrete bridges. PCI J 1998;43(5):88–101.

[29] Wu T, Sun Y, Liu X, Cao Y. Comparative study of the flexural behavior of steel fiber-reinforced lightweight aggregate concrete beams reinforced and prestressed with CFRP tendons. Eng Struct 2021;233:111901.

[30] Wang X, Shi J, Wu G, Yang L, Wu Z. Effectiveness of basalt FRP tendons for strengthening of RC beams through the external prestressing technique. Eng Struct 2015;101:34–44.

[31] Yuan A, He Y, Dai H, Cheng L. Experimental study of precast segmental bridge box girders with external unbonded and internal bonded posttensioning under monotonic vertical loading. J Bridge Eng 2015;20(4):04014075.

[32] Takebayashi T, Deeprasertwong K, Leung YW. A Full-Scale Destructive Test of a Precast Segmental Box Girder Bridge with Dry Joints and External Tendons. Proc Inst Civ Eng-Struct Build 1994;104(3):297–315.

[33] Turmo J, Ramos G, Aparicio AC. FEM modelling of unbonded post-tensioned segmental beams with dry joints. Eng Struct 2006;28(13):1852–63.

[34] Tran DT, Pham TM, Hao H, Do TV, Tran TT. Blast behaviour of precast segmental vs monolithic concrete beams prestressed with unbonded tendons: A numerical investigation. Int J Impact Eng 2023;173:104434.

[35] DTMR. Design Criteria for Floating Walkways and Pontoons. Brisbane, Queensland: Queensland Department of Transport and Main Roads,; 2015.

[36] DTMR. (2019). Transport and Main Roads Specifications, MRTS72, Manufacture of Precast Concrete Elements.

[37] DTMR. (2022). Transport and Main Roads Specifications MRTS70 Concrete, Transport and Main Roads Specifications.

[38] Standards Australia. (2018). AS3600: 2018—Concrete Structures.

[39] Australia, S. (2014). Methods of Testing Concrete-Compressive Strength Tests-Concrete, Mortar and Grout Specimens. AS1012.9. Sydney. New South Wales, Australia: Standards Australia.

[40] Canadian Standards Association. (2019). Specification for fibre-reinforced polymers (CAN/CSA S807–19). Rexdale, ON, Canada.

[41] ASTM, D. Standard Test Method for Tensile Properties of Fiber-reinforced Polymer Matrix Composite Bars. ASTM,; 2011. D7205-11.

[42] Alajarmeh O, Manalo A, Benmokrane B, Ferdous W, Mohammed A, Abousnina R, et al. Behavior of circular concrete columns reinforced with hollow composite sections and GFRP bars. Mar Struct 2020;72:102785.

[43] ASTM, D. Standard Test Method for Ignition Loss of Cured Reinforced Resins. ASTM,; 2018. D2584-18.

[44] Liu T, Feng P, Bai Y, Bai S, Yang JQ, Zhao F. Flexural performance of curved-pultruded GFRP arch beams subjected to varying boundary conditions. Eng Struct 2024;308:117962.

[45] American Concrete Institute. Prestressing Concrete Structures with Frp Tendons. Farmington Hills, Michigan: American Concrete Institute,; 2004.

[46] Zhang W, Zhang S, Wei J, Huang Y. Flexural behavior of SFRC-NC composite beams: an experimental and numerical analytical study. Structures, Vol. 60. Elsevier,; 2024, 105823.

[47] Huang H, Li M, Zhang W, Yuan Y. Seismic behavior of a friction-type artificial plastic hinge for the precast beam–column connection. Arch Civ Mech Eng 2022;22 (4):201.

[48] Luo Y, Liu X, Chen F, Zhang H, Xiao X. Numerical simulation on crack–inclusion interaction for rib-to-deck welded joints in orthotropic steel deck. Metals 2023;13 (8):1402.

[49] Chen F, Zhang H, Li Z, Luo Y, Xiao X, Liu Y. Residual stresses effects on fatigue crack growth behavior of rib-to-deck double-sided welded joints in orthotropic steel decks. Adv Struct Eng 2024;27(1):35–50.

[50] American Concrete Institute. Guide for the design and construction of structural concrete reinforced with fiber-reinforced polymer (FRP) bars. Farmington Hills, Michigan: American Concrete Institute,; 2015.

[51] Krall M, Polak MA. Concrete beams with different arrangements of GFRP flexural and shear reinforcement. Eng Struct 2019;198:109333.

[52] Abed F, El-Chabib H, AlHamaydeh M. Shear characteristics of GFRP-reinforced concrete deep beams without web reinforcement. J Reinf Plast Compos 2012;31 (16):1063–73.

[53] Maranan GB, Manalo AC, Benmokrane B, Karunasena W, Mendis P, Nguyen TQ. Shear behaviour of geopolymer-concrete beams transversely reinforced with continuous rectangular GFRP composite spirals. Compos Struct 2018;187:454–65.

[54] Jiang H, Chen L, Ma ZJ, Feng W. Shear behavior of dry joints with castellated keys in precast concrete segmental bridges. J Bridge Eng 2015;20(2):04014062.

[55] AASHTO. (2003). Interim revisions to the guide specifications for the design and construction of segmental concrete bridges, (1999).

[56] Fu C, Zhu Y, Wang Y. Stiffness assessment of cracked post-tensioned concrete beams with unbonded tendons based on the cracking pattern. Eng Struct 2020;214: 110599.

[57] Systèmes D. Abaqus/CAE User's Manual. Providence, RI, USA: Dassault Systèmes Simulia Corp,; 2019.

[58] ACI Committee. Building Code Requirements for Structural Concrete (ACI 318-08) and Commentary. American Concrete Institute,; 2008.

[59] Papanikolaou VK, Kappos AJ. Confinement-sensitive plasticity constitutive model for concrete in triaxial compression. Int J Solids Struct 2007;44(21):7021–48.

[60] Carreira DJ, Chu KH. Stress-strain relationship for plain concrete in compression. J Proc 1985;Vol. 82(No. 6):797–804.

[61] Sayed-Ahmed EY, Shrive NG. A new steel anchorage system for post-tensioning applications using carbon fibre reinforced plastic tendons. Can J Civ Eng 1998;25 (1):113–27.

[62] Pournoori, N., García, O.R., Jokinen, J., Hokka, M., & Kanerva, M. (2021). Homogenization effects on simulated pultruded glass fibre reinforced laminate under compression–from static to dynamic models. In EPJ Web of Conferences (Vol. 250, p. 02034). EDP Sciences.

[63] Lam D, Dai XH, Han LH, Ren QX, Li W. Behaviour of inclined, tapered and STS square CFST stub columns subjected to axial load. Thin-Walled Struct 2012;54: 94–105.

[64] Mohamad ME, Ibrahim IS, Abdullah R, Rahman AA, Kueh ABH, Usman J. Friction and cohesion coefficients of composite concrete-to-concrete bond. Cem Concr Compos 2015;56:1–14.

[65] Obaidat YT, Heyden S, Dahlblom O. The effect of CFRP and CFRP/concrete interface models when modelling retrofitted RC beams with FEM. Compos Struct 2010;92(6):1391–8.

[66] PCI. Design Handbook. 6th ed.,. Chicago, IL: Precast/Prestressed Concrete Institute,; 2004.

[67] AASHTO LRFD. Bridge Construction Specifications. 6th edition.,. Washington, DC: American Association of State Highway and Transportation Officials,; 2012.

[68] Naaman, A.E. (1991). Stress at ultimate in unbonded prestressing tendons by strain compatibility. In Progress in Structural Engineering: Proceedings of an international workshop on progress and advances in structural engineering and mechanics, University of Brescia, Italy, September 1991 (pp. 217–227). Dordrecht: Springer Netherlands.

[69] Alkhairi, F.M. (1991). On the flexural behavior of concrete beams prestressed with unbonded internal and external tendons (Doctoral dissertation, University of Michigan).